

# A study of X-ray observations of Aquila X-1

Kelsey L. Hoffman

Master of Science

Department of Physics

McGill University

Montreal, Quebec

2006 - 10 -04

A thesis submitted to McGill University in partial fulfillment of the requirements of  
the degree of Master of Science

©Kelsey Hoffman, 2006



Library and  
Archives Canada

Bibliothèque et  
Archives Canada

Published Heritage  
Branch

Direction du  
Patrimoine de l'édition

395 Wellington Street  
Ottawa ON K1A 0N4  
Canada

395, rue Wellington  
Ottawa ON K1A 0N4  
Canada

*Your file* *Votre référence*  
*ISBN: 978-0-494-28493-3*  
*Our file* *Notre référence*  
*ISBN: 978-0-494-28493-3*

#### NOTICE:

The author has granted a non-exclusive license allowing Library and Archives Canada to reproduce, publish, archive, preserve, conserve, communicate to the public by telecommunication or on the Internet, loan, distribute and sell theses worldwide, for commercial or non-commercial purposes, in microform, paper, electronic and/or any other formats.

The author retains copyright ownership and moral rights in this thesis. Neither the thesis nor substantial extracts from it may be printed or otherwise reproduced without the author's permission.

#### AVIS:

L'auteur a accordé une licence non exclusive permettant à la Bibliothèque et Archives Canada de reproduire, publier, archiver, sauvegarder, conserver, transmettre au public par télécommunication ou par l'Internet, prêter, distribuer et vendre des thèses partout dans le monde, à des fins commerciales ou autres, sur support microforme, papier, électronique et/ou autres formats.

L'auteur conserve la propriété du droit d'auteur et des droits moraux qui protègent cette thèse. Ni la thèse ni des extraits substantiels de celle-ci ne doivent être imprimés ou autrement reproduits sans son autorisation.

---

In compliance with the Canadian Privacy Act some supporting forms may have been removed from this thesis.

Conformément à la loi canadienne sur la protection de la vie privée, quelques formulaires secondaires ont été enlevés de cette thèse.

While these forms may be included in the document page count, their removal does not represent any loss of content from the thesis.

Bien que ces formulaires aient inclus dans la pagination, il n'y aura aucun contenu manquant.

  
**Canada**

## DEDICATION

For my dad.

## ACKNOWLEDGEMENTS

I would like to thank my supervisor, Bob Rutledge, for the opportunity to challenge myself and expand my knowledge immensely. I would also like to thank Marjorie, without whom I would have had to sleep on the street that one time. Also for her patient explanations. A special thank you to my band, my fans and the knitting circle for the continuing support. I am extremely grateful to my mom, Marvin, Ken, Steve, and Oreo for unceasing love and support.

## ABSTRACT

The goal of this thesis is to obtain the most precise radius measurement of the neutron star in Aql X-1. In order to measure the radius, nine new observations have been analyzed along with four previously analyzed observations. Two of the new observations were taken with *XMM-Newton*. During the times of the *XMM-Newton* observations Aql X-1 was found not to be in quiescence and so cannot be used for radius measurements. This state of active accretion of Aql X-1 is characterized by basic spectral analysis. Spectral lines from Aql X-1 were investigated using the Reflection Grating Spectrometer (RGS) on *XMM-Newton*. There was no visual evidence of spectral lines from Aql X-1 observed. The seven new *Chandra* observations along with four others all caught Aql X-1 in quiescence. These observations were taken over two quiescent periods with an intervening outburst. Joint spectral fitting of the 11 observations revealed significant variability in the high energy ( $>2\text{keV}$ ) emission but that the thermal emission – which emerges from the neutron star atmosphere – was constant, as expected from theory. The high energy component was parameterized with a varying power-law, with the thermal component held constant. The best fit from jointly fitting the observations was  $R_\infty = 11.6^{+0.4}_{-0.1} (D/5\text{kpc})\text{km}$  and  $\text{Log}T_{eff}(\text{K}) = 6.49^{+0.01}_{-0.02}$ , where  $D$  is the distance to Aql X-1. This is the most precise measurement of the neutron star radius for this source, with the dominant uncertainty (not included in the statistical uncertainty) now in the source distance. Finally, a new class of neutron stars, RRATs, have recently been introduced. One of the RRATs includes Aql X-1 in its error circle. A search was performed of the

*Chandra* and *XMM-Newton* observations for candidate counterparts. A fading X-ray source, CXOU J191121.4+003844 , was found to lie within the error circle of the RRAT, which is put forth as a candidate X-ray counterpart.

## ABRÉGÉ

Le but de cette thèse est de mesurer le plus précisément possible le rayon de l'étoile à neutrons Aql X-1. Pour ce faire, nous avons analysé neuf nouvelles observations en plus de quatre autres ayant déjà fait l'objet d'analyses ultérieures. Deux des nouvelles observations furent obtenues avec *XMM-Newton* au cours desquels Aql X-1 n'était pas en dormance. Pour cette raison, nous n'avons pu utiliser ces données pour mesurer le rayon. Cet état d'accrétion active de Aql X-1 fut caractérisé par une analyse spectroscopique élémentaire. Nous avons cherché la présence de raies spectrales à l'aide du Reflection Grating Spectrometer (RGS) sur *XMM-Newton*. Aucun signe de raies spectrales ne fut détecté. Les sept observations restantes, obtenues avec *Chandra*, de même que les quatre autres observations, ont toutes été réalisées alors que Aql X-1 était en dormance. Ces observations couvrent deux périodes de dormance séparées par un sursaut d'activités. L'ajustement simultané de modèles spectraux sur les 11 observations révèle une variabilité de l'émission à haute énergie ( $>2\text{keV}$ ). Toutefois, la composante thermique, qui provient de l'atmosphère de l'étoile à neutrons, s'avère constante tel que prédit par la théorie. La composante à haute énergie est paramétrisée par une loi de puissance variable alors que la composante thermique est maintenue constante. Les meilleures paramètres obtenus pour l'ajustement spectral sont:  $R_\infty = 11.6_{-0.1}^{+0.4} (D/5\text{kpc})\text{km}$  and  $\text{Log}T_{eff}(\text{K}) = 6.49_{-0.02}^{+0.01}$ , où  $D$  est la distance nous séparant de Aql X-1. Il s'agit de la mesure du rayon de Aql X-1 la plus précise effectuée jusqu'à ce jour, avec la distance comme principale source d'incertitude (non

incluse ici dans l'erreur statistique). Finalement, une nouvelle classe d'étoiles à neutrons, les RRATs, a récemment été introduite. En tenant compte de l'incertitude sur sa position, l'un de ces RRATs se trouve à proximité de Aql X-1. La recherche d'une contrepartie dans nos données *Chandra* et *XMM-Newton* a été effectuée. Nous avons détecté une source de rayons X dont la luminosité décroît, CXOU J191121.4+003844, coïncidente avec le cercle d'erreur sur la position du RRAT et nous proposons qu'il s'agisse de la contrepartie rayons X.

## TABLE OF CONTENTS

DEDICATION . . . . .		ii
ACKNOWLEDGEMENTS . . . . .		iii
ABSTRACT . . . . .		iv
ABRÉGÉ . . . . .		vi
LIST OF TABLES . . . . .		xi
LIST OF FIGURES . . . . .		xii
1 Introduction . . . . .		1
1.1 Neutron Stars and the Dense Matter Equation of State . . . . .		1
1.2 Low Mass X-ray Binaries . . . . .		4
1.3 Neutron Star Radius Measurements . . . . .		5
1.4 Aquila X-1 Overview . . . . .		9
2 Satellites . . . . .		13
2.1 Introduction . . . . .		13
2.2 <i>XMM-Newton</i> . . . . .		14
2.2.1 History and Telescope overview . . . . .		14
2.2.2 Instruments . . . . .		16
2.2.3 <i>XMM-Newton</i> Data Preparation . . . . .		20
2.3 <i>Chandra</i> . . . . .		22
2.3.1 History and Telescope overview . . . . .		22
2.3.2 Instruments . . . . .		23
2.3.3 Data Preparation . . . . .		24
2.4 <i>RXTE</i> All-Sky Monitor . . . . .		26
2.5 Summary . . . . .		27

3	<i>XMM-Newton</i> Observations of Aql X-1 . . . . .	28
3.1	Introduction . . . . .	28
3.1.1	Global Lightcurve of Aql X-1 . . . . .	29
3.2	Observations and Data Reduction . . . . .	30
3.3	Statistical Methods . . . . .	32
3.4	Analysis . . . . .	33
3.5	Results . . . . .	39
3.6	Discussion and Conclusions . . . . .	40
4	High Resolution Spectroscopy . . . . .	44
4.1	Introduction . . . . .	44
4.2	Observations and data reduction . . . . .	45
4.3	Analysis . . . . .	46
4.4	Results . . . . .	49
4.5	Discussion . . . . .	49
5	Radius Measurements . . . . .	54
5.1	Introduction . . . . .	54
5.2	Hydrogen Atmosphere Model . . . . .	54
5.3	Observations and Data Reduction . . . . .	57
5.4	Analysis . . . . .	57
5.5	Results . . . . .	59
5.5.1	Individual Observation Spectral fits . . . . .	59
5.5.2	Multiple Observation Spectral fits . . . . .	60
5.6	Discussion . . . . .	64
6	RRATs . . . . .	70
6.1	Introduction . . . . .	70
6.2	Observations and Analysis . . . . .	72
6.3	Results . . . . .	73
6.3.1	<i>Chandra</i> Source Search . . . . .	73
6.3.2	CXOU J191121.4+003844 . . . . .	74
6.3.3	Aql X-1 . . . . .	81
6.4	Discussion . . . . .	81

7	Conclusions . . . . .	84
7.1	<i>XMM-Newton</i> Observations . . . . .	84
7.2	Search for Spectral lines . . . . .	84
7.3	Radius Measurements . . . . .	84
7.4	RRATs . . . . .	86
	Appendix: Abbreviations . . . . .	87

LIST OF TABLES

<u>Table</u>	<u>page</u>
1-1 Sample of radius measurements of neutron stars using a hydrogen atmosphere model . . . . .	10
2-1 Overview of various X-Ray Telescopes . . . . .	15
2-2 Overview of <i>XMM-Newton</i> Characteristics . . . . .	17
3-1 All <i>XMM-Newton</i> and <i>Chandra</i> observations of Aql X-1 used in thesis	30
3-2 Spectral Fits of Aql X-1 from the two <i>XMM-Newton</i> observations . . .	41
3-3 Spectral Fits of Aql X-1 from the two <i>XMM-Newton</i> observations continued . . . . .	42
4-1 Energies Ignored in RGS spectral fits . . . . .	48
4-2 Spectral fits for the two <i>XMM-Newton</i> observations . . . . .	52
5-1 Best fit H-atmosphere model parameters to individual <i>Chandra</i> obser- vations of Aql X-1 . . . . .	62
5-2 Spectral Parameters for All <i>Chandra</i> observations of Aql X-1 with varying power-law spectral component . . . . .	67
6-1 Sources detected in <i>Chandra</i> Observation 709 . . . . .	74
6-2 Spectral fits to CXOU J191121.4+003844 . . . . .	77
6-3 CXOU J191121.4+003844 source and background counts in both <i>XMM-Newton</i> observations . . . . .	80

## LIST OF FIGURES

<u>Figure</u>	<u>page</u>
1-1 A sample of neutron star equation of states . . . . .	3
2-1 Schematic of <i>XMM-Newton</i> satellite . . . . .	16
2-2 Energy resolution of RGS units on <i>XMM-Newton</i> . . . . .	19
2-3 Schematic of <i>Chandra</i> . . . . .	23
2-4 Focal plane of ACIS on <i>Chandra</i> . . . . .	24
2-5 Energy resolution of ACIS pre-launch on <i>Chandra</i> . . . . .	25
3-1 Luminosity of Aql X-1 from <i>XMM-Newton</i> and <i>Chandra</i> observations compared to the All-Sky monitor . . . . .	31
3-2 Looking for background flaring in <i>XMM</i> observation XMM-1 . . . . .	34
3-3 Looking for background flaring in <i>XMM</i> observation XMM-2 . . . . .	35
3-4 Lightcurve of Aql X-1 from XMM-1 observation . . . . .	37
3-5 Lightcurve of Aql X-1 from XMM-2 observation . . . . .	38
4-1 Photon dispersion on RGS1 . . . . .	46
4-2 Background lightcurves of RGS1 and RGS2 for XMM-1 . . . . .	47
4-3 Spectral fit of RGS2 from XMM-2 to an absorbed disk blackbody . . . . .	50
4-4 Spectral fit of RGS1 from XMM-2 to an absorbed disk blackbody . . . . .	51
5-1 Individual spectral fits of 11 <i>Chandra</i> observations to an absorbed hydrogen atmosphere . . . . .	61
5-2 Summary of best fit H-atmosphere model parameters to individual <i>Chandra</i> observation of Aql X-1 . . . . .	63

5-3	All 11 extracted spectra of Aql X-1 from <i>Chandra</i> . . . . .	65
5-4	Joint spectral fits of 11 <i>Chandra</i> observations to an absorbed hydrogen atmosphere with a power-law . . . . .	66
5-5	Variability of the power-law component in the 11 <i>Chandra</i> observations of Aql X-1 . . . . .	68
6-1	The PI channels from <i>Chandra</i> 709 of Aql X-1, the background and CXOU J191121.4+003844 . . . . .	75
6-2	Best fit spectral model to CXOU J191121.4+003844 . . . . .	78
6-3	PI Channels from Aql X-1 and the background from all <i>Chandra</i> observations . . . . .	82

## CHAPTER 1 Introduction

### 1.1 Neutron Stars and the Dense Matter Equation of State

Neutron stars are formed by the collapse of the core of a star with mass  $>8$  solar masses ( $M_{\odot}$ )<sup>1</sup>. The basic properties of neutron stars are a mass of  $\sim 1.5M_{\odot}$ , a radius of  $\sim 12$  km and a density greater than the density measurement of protons and neutrons in laboratory nuclei (for a general review of neutron stars see Lattimer & Prakash (2004)). There are five structural regions of a neutron star: the inner and outer cores, the crust, the envelope and the atmosphere. The inner and outer cores of a neutron star are the largest region: for a neutron star of  $\sim 12$  km the inner and outer cores encompass an inner region of  $\sim 10$  km. The two cores constitute  $\sim 99\%$  of the neutron star mass. Nucleons, electrons and muons compose the outer core, while the inner core could contain exotic matter such as strange quark matter. The crust extends for 1-2 km below the neutron star surface and contains primarily nuclei. The nuclei in the crust varies with density, with the number of neutrons increasing with density. The transition from crust to core occurs when the density approaches nuclear density – that is, when the individual nuclei in the crust are pressed so close together that they become undifferentiated nuclear matter. Though the envelope

---

<sup>1</sup> The upper limit of initial mass is dependent on metallicity, see Heger et al. (2003)

and atmosphere contain a negligible amount of the overall neutron star's mass, they both influence the spectrum observed. The envelope influences the transport of the thermal energy from the surface and the atmosphere influences the observed photon spectra emitted from the neutron star.

The dense matter equation of state (dEOS) relates the pressure and density of matter in the center of the neutron star at densities near and above nuclear density ( $\geq 0.16$  baryons  $\text{fm}^{-3}$ ). From the dEOS neutron star properties such as the mass-radius relation can be determined (the dEOS and neutron star structure are reviewed in Lattimer & Prakash (2001)). There are a large number of proposed dEOSs due to theoretical uncertainties. Many body interactions at high densities are not well constrained observationally leading to a variety of dEOSs. Also, the variety of dEOS results from a poor understanding of strong interactions and neutron star composition is dependent on these interactions. Even though nuclear matter in the laboratory is well understood, neutron star matter differs in that nuclear matter is nearly equal in neutrons and protons, while neutron star matter only has a small percent of protons (Lattimer & Prakash, 2004).

A sample of the mass-radius relationships for various equations of state is shown in Figure 1-1 (from Lattimer & Prakash, 2004). The dEOSs displayed are both for "normal" neutron stars composed of hadronic matter, as well as more exotic dEOSs, such as neutron stars composed of strange quark matter (SQM1 and SQM2). Figure 1-1 displays the limits placed on the mass-radius relationship of neutron stars via causality and rotation arguments. The causality argument, that the speed of sound cannot exceed the speed of light in the dense neutron star, sets a lower limit to

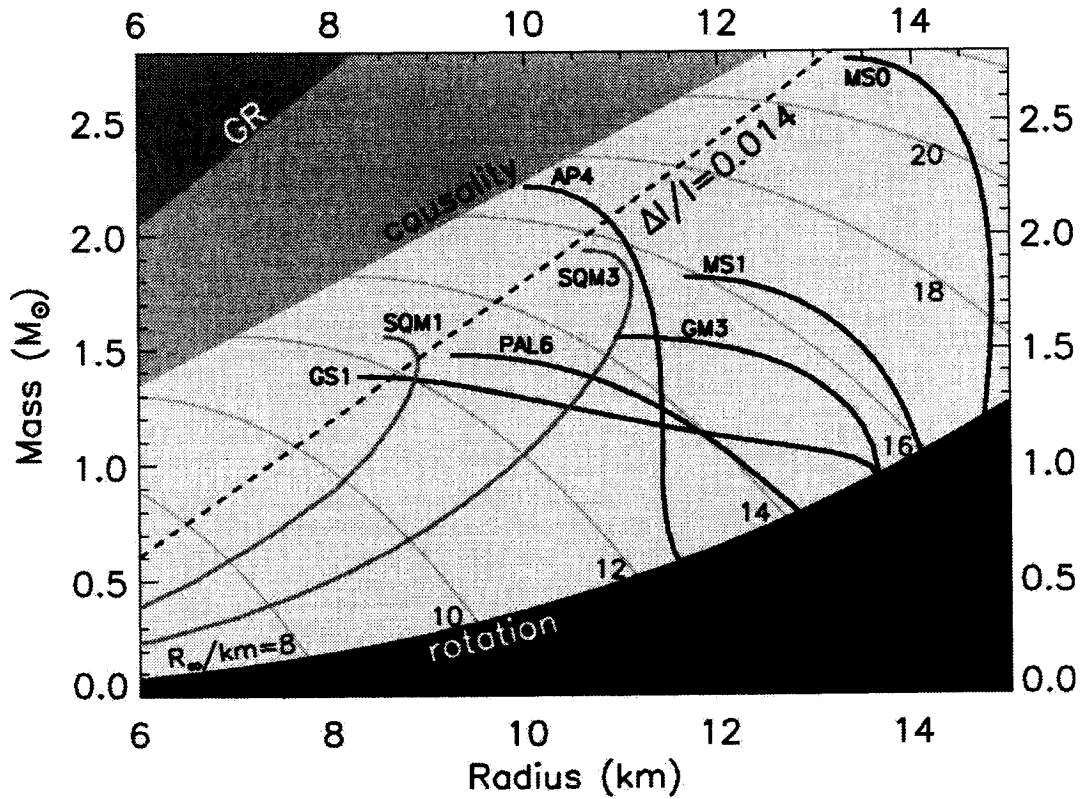


Figure 1-1: A sample of mass-radius relationships for neutron stars based on different proposed dEOSs. The SQM1, and SQM3 are equations of state for strange quark matter. The other curves are for normal matter (Lattimer & Prakash, 2004). Lines of constant radiation radius,  $R_\infty$ , and limits from causality and rotation are shown.

the neutron star radius (Lattimer & Prakash, 2001). The rotation limit is derived from the mass-shedding limit, where the velocity of the neutron star surface and a gravitationally bound particle just above the surface are equal (Lattimer & Prakash, 2004). The maximum rotation for a neutron star is the mass-shedding limit, a neutron star rotating above the mass-shedding limit begins to lose mass.

Using Figure 1-1, a simultaneous measurement of radius and mass of a neutron star would indicate acceptable dEOSs. A measurement of either mass or radius alone

places limits on which dEOS describes dense matter at the center of a neutron star. Masses of neutron stars have been measured using orbital doppler shift measurements of pulsars (Thorsett & Chakrabarty, 1999) to a precision of  $\leq 0.01\%$ . The methods of determining the radius of neutron stars are discussed in detail in section 1.3. Some of the ways that can be used to determine radii are through the neutron star's thermal spectrum, absorption lines or photospheric expansion. Low Mass X-ray binaries provide an excellent environment for radius measurements, as they can produce the three features mentioned above.

## 1.2 Low Mass X-ray Binaries

A general overview of Low Mass X-ray Binaries (LMXBs) is covered in White et al. (1995). An X-ray binary consists of either a neutron star or a black hole which is accreting material from its companion star. A LMXB is a type of X-ray binary where the companion star is a type A or later and mass is transferred to the compact object via Roche lobe overflow. By detecting a type I X-ray burst in an LMXB the compact object is determined to be a neutron star. A type I burst is due to thermonuclear flashes occurring on the surface of the neutron star. Whereas, a type II burst is due to accretion instabilities in the binary. A characteristic of the neutron stars in LMXBs is a weak magnetic fields. Weak magnetic fields for LMXBs have been derived from the lack of X-ray pulsations: a neutron star with a strong magnetic field would funnel accretion material onto the poles, a misaligned magnetic and rotation axis would result in X-ray pulsations.

A subclass of LMXB is the Soft X-ray Transient (SXT). SXTs are normally in a state of quiescence, when there is little or no accretion. However, at times, there may

be an increase in the accretion rate where the SXTs will outburst. This outburst is due to the dwarf-nova instability (see Lasota, 2001). The outburst can last from weeks to months. The observed quiescent luminosity for most neutron star SXTs is in the range of  $10^{32}$ - $10^{34}$  erg s<sup>-1</sup> but when in outburst this luminosity increases to  $10^{36}$ - $10^{38}$  erg s<sup>-1</sup> (Cackett et al., 2005). While the neutron star is in quiescence it emits thermal radiation. The thermal emission from the neutron star while in quiescence has been explained to be a result of “deep crustal heating” (Brown et al., 1998). In deep crustal heating, nuclear reactions occur in the crust while accretion onto the neutron star is active. The core reaches a steady state where heat deposited during accretion outbursts is equal to the heat radiated when the neutron star is in quiescence. The time for the core to reach thermal equilibrium is  $\sim 10^4$  years (Brown et al., 1998; Colpi et al., 2000). The luminosity emitted by the neutron star while it is in quiescence by deep crustal heating is given by:

$$L_q = 6 \times 10^{32} \left( \frac{\langle \dot{M} \rangle}{10^{-11} M_\odot \text{yr}^{-1}} \right) \text{ ergs s}^{-1}, \quad (1.1)$$

where  $\langle \dot{M} \rangle$  is the time-averaged accretion rate (Brown et al., 1998). This quiescent thermal radiation makes it possible for a neutron star to be observed when it is not actively accreting. Observing a neutron star in quiescence is a key requirement for one method of determining a radius.

### 1.3 Neutron Star Radius Measurements

Obtaining an accurate ( $\leq \pm 5\%$ ) mass and radius measurement for a neutron star would greatly constrain the dEOS. Mass measurements of neutron stars can be made with accuracy to  $\sim 10^{-4}$  from radio pulsars. An example of such accuracy

is in the mass measurements of the double neutron star binary system of 1913+16 (Thorsett & Chakrabarty, 1999). There is a possibility that neutron stars in X-ray binaries have larger masses than those measured in radio binaries. This possible mass difference would be due to X-ray binaries accreting more mass since formation than the radio binaries (Lattimer & Prakash, 2001). Since the mass of a neutron star can be accurately measured, it becomes important to obtain radius measurements. Mass measurements alone can limit which dEOSs are acceptable, but this would still include a range of radii. A radius measurement would even further limit dEOSs that describe neutron star matter. There are various methods which can be used for radius measurements:

**Thermal Emission** : A reliable estimate of neutron star radius is through atmospheric emission. The luminosity and temperature of the neutron star's thermal emission is redshifted resulting in a measurement of a radiation radius,  $R_\infty = R_\star / \sqrt{1 - 2GM_\star/c^2 R_\star} = R_\star / g_r$ , where  $R_\star$  is the physical radius of the neutron star,  $G$  is the gravitational constant,  $c$  is the speed of light,  $M_\star$  is the neutron star mass and  $g_r$  is the gravitational redshift (Lattimer & Prakash, 2001). Treating the thermal emission as resulting from a hydrogen atmosphere gives a more realistic radius measurement than treating the neutron star as a blackbody. The blackbody model in the case of neutron stars is based on a typically invalid physical assumption of opacity of the neutron star atmosphere. The spectra of an atmosphere and a blackbody model are different, specifically the blackbody model overestimates the effective temperature of the neutron star, thereby underestimating the radius (Zavlin et al., 1996). The

radius is determined from the luminosity and temperature of the neutron star:  $R_{\star}^2 \propto L/T^4$ , where  $L$  is the luminosity and  $T$  is the temperature. The luminosity determination is dependent on distance to the neutron star.

**Photospheric Expansion** : The atmosphere of the neutron star expands during a type I burst (Lewin et al., 1995). The peak luminosities of the strong bursts are close to the Eddington luminosity  $L \simeq L_{ED} \propto M/g_r$ , the neutron star radius can be calculated from the redshift factor,  $g_r$  (Pavlov et al., 1991).

**Absorption Lines** : The matter that produces the absorption lines is either from the companion star in a binary or from nuclear burning during a burst (Lattimer & Prakash, 2001). By measuring the gravitational redshift of the spectral lines arising from the photosphere, radius measurements of the neutron star can be made assuming a mass (Cottam et al., 2002). The gravitational redshift is measured by relating the observed line wavelength ( $\lambda_o$ ) and the wavelength as it was emitted at the source ( $\lambda_e$ ):  $g_r = \lambda_o/\lambda_e \approx M_{\star}/R_{\star}(G/c^2)$ .

**Pressure Broadening of Absorption Lines** The pressure broadening of absorption lines resulting from the Stark effect gives a width  $\Delta \propto M_{\star}/R_{\star}^2$ . The Stark effect is the splitting of spectral lines due to the presence of an electric field. A gravitational redshift measurement from absorption lines (see above) in the same observation gives another relation of mass and radius:  $g_r \approx M_{\star}/R_{\star}(G/c^2)$ . Coupling the two measurements the radius of the neutron star can be determined separately, independent of distance (Paerels, 1997).

**Laboratory measurements** : The radius of neutron stars can be determined by the pressure of isospin asymmetric nuclear matter in a terrestrial laboratory.

The pressure of isospin asymmetric matter is proportional to the slope of the symmetry energy of nuclear matter (Li & Steiner, 2005). The symmetry energy function results from a quadratic interpolation of the asymmetry energy as function of proton fraction:  $E(n,x)=E(n,x=1/2)+S_\nu(n)(1-2x)^2$ . Where  $S_\nu(n)$  is the symmetry energy function and  $x$  is the proton fraction. For nuclear matter  $x \simeq 1/2$ , an almost equal number of protons and neutrons. For a neutron star the proton fraction is a few percent (Lattimer & Prakash, 2004). The symmetry energy is approximately proportional to density (Lattimer & Prakash, 2001), assuming a neutron star mass results in a radius measurement from  $S_\nu$ .

**Pulse fractions, QPOs, and Glitches** : An attempt to use pulse fractions and light curves for radius determination suggested radii on the order of 15km. Though radii were determined, this method was unsuccessful at calculating pulse fractions and light curves which were in agreement to observation. Quasi-Periodic Oscillations (QPOs) may be able to provide limits on the neutron star mass and radius. Glitches are related to the internal moment of inertia of neutron stars, constraints to mass and radius may be provided through frequencies and sizes of the glitches (Lattimer & Prakash, 2001).

Photospheric expansion has the advantage that it is a process of the neutron star's photosphere instead of the accretion disk. But, photospheric expansion is limited by uncertainties in: source distance, anisotropy of burst emission, and the spectra emitted (van Paradijs & Lewin, 1987). The combination of using gravitational redshift measured from absorption lines and pressure broadening of absorption lines has the advantage that is it independent of distance but requires a level of emission

from the source that can be detected and also a confident identification of the spectral lines (Paerels, 1997). The method of modeling the thermal emission of a neutron star with a hydrogen atmosphere is useful for neutron stars in a state of quiescence and the dominate uncertainty in this method is in the distance measurement.

In the case of normal neutron stars within the mass range of  $1-1.5M_{\odot}$  some dEOSs display a similar characteristic, in that the radius is relatively constant as a function of mass. Since the neutron star radius can be relatively independent of the neutron star mass (Lattimer & Prakash, 2001) one of the biggest uncertainties in determining the radius is the uncertainty in the distance to the neutron star. Observing neutron stars in globular clusters decreases the distance uncertainty. Table 1–1 is a list of some radius measurements of neutron stars,  $\omega$  Cen and M13 are quiescent neutron stars in these globular clusters. Both Aql X-1 and Cen X-4 are in the galactic plane. The radius measurements of the four neutron stars listed in Table 1–1 were determined using a hydrogen atmosphere model.

As Aql X-1 is one of the brightest known examples of a quiescent emitter and had been well observed, Aql X-1 provides an excellent source for radius determination using the hydrogen atmosphere model. With multiple observations of Aql X-1 it also becomes possible to search for, study and characterize systematic uncertainties in the radius determination.

#### 1.4 Aquila X-1 Overview

Aql X-1 is a SXT LMXB. It is located at the coordinates 19:11:16.0+00:35:06 (Ebisawa et al., 2003). Type I bursts from Aql X-1 were detected indicating that the X-ray binary contains a neutron star (Koyama et al., 1981). The companion to

Table 1–1: Sample of radius measurements of neutron stars using a hydrogen atmosphere model

Neutron Star	Radius (km)	Reference
$\omega$ Cen	$14.3 \pm 2.1(D/5\text{kpc})$	1
	$13.6 \pm 0.3(D/5.3\text{kpc})$	2
M13	$12.8 \pm 0.4(D/7.7\text{kpc})$	3
Aql X-1	$13.4^{+5}_{-4}(D/5\text{kpc})$	4
Cen X-4	$12.9 \pm 2.6(D/1.2\text{kpc})$	5

$\omega$  Cen and M13 are neutron stars in globular clusters and Aql X-1 and Cen X-4 are in the plane.

References: (1) Rutledge et al. (2002a); (2) Gendre et al. (2003b); (3) Gendre et al. (2003a); (4) Rutledge et al. (2001a); (5) Rutledge et al. (2001b)

Aql X-1 has been identified as a spectral type K7 star (Chevalier et al., 1999). The minimum distance to Aql X-1 is 4kpc, while the maximum is 6.4kpc (Welsh et al., 2000; Rutledge et al., 2001a). A distance value of 5kpc for Aql X-1 is used throughout this thesis. Aql X-1 has an orbital period of 18.95 hours (Welsh et al., 2000). Aql X-1 has frequent outbursts, the recurrence of Aql X-1 is approximately yearly (Priedhorsky & Terrell, 1984). X-ray outburst from Aql X-1 have been observed on many occasions with X-ray satellites such as *UHURU* (Kaluzienski et al., 1977), *Hakucho* (Koyama et al., 1981), seven outbursts detected with *Vela 5B* (Priedhorsky & Terrell, 1984), *Einstein* (Czerny et al., 1987), *BATSE* (Harmon et al., 1996) and *RXTE* in 1998, 1999, 2000, and 2005 (Cui et al., 1998; Maccarone & Coppi, 2003; Maitra & Bailyn, 2004; Rodriguez et al., 2006). And Aql X-1 has been previously detected in quiescence nine times, once with *EXOSAT* (van Paradijs et al., 1987), twice with *ROSAT* (Verbunt et al., 1994), once with *ASCA* (Asai et al., 1998), once with *BeppoSAX* (Campana & Stella, 2003) and four times with *Chandra* (Rutledge et al., 2001a, 2002b). Previous radius measurements from the spectra of Aql X-1

with an absorbed hydrogen atmosphere plus a power-law component for a radiation radius of  $R_\infty = 13.4_{-4}^{+5} (D/5\text{kpc})\text{km}$  (Rutledge et al., 2001a). It is the precision of this measurement we intend to improve upon in the present work.

In this thesis nine new X-ray observations taken to study Aql X-1 and improve its radius measurement are analyzed. Two of the new X-ray observations were taken with *XMM-Newton*, the other seven were taken with *Chandra*. The two *XMM-Newton* observations were taken within  $\sim 1$  week of each other and failed to catch Aql X-1 in quiescence. Nonetheless, X-ray properties of Aql X-1 at lower accretion-driven X-ray luminosities than previously observed ( $L_x \sim 10^{36} \text{ erg s}^{-1}$ ) are characterized through basic analysis. The seven new *Chandra* observations were combined with four previously analyzed observations. All 11 observations caught Aql X-1 in quiescence. Through analysis of the *Chandra* observations the measured neutron star radius for Aql X-1 is improved upon. Intensity variability of Aql X-1 while in quiescence is found to be driven by variability of a high energy ( $\geq 2\text{keV}$ ) component, not the thermal component. Throughout this work only non-magnetized models are used and the neutron star mass is assumed to be  $1.4M_\odot$ .

This first chapter has given a general overview of neutron stars, low-mass X-ray binaries, methods for measuring the radius of neutron stars, and properties of Aql X-1. The following chapter discusses the specifics of the satellites that were used in order to obtain the observations of Aql X-1 analyzed in this thesis work. Observations of Aql X-1 taken with the satellites *XMM-Newton* and *Chandra* were used in this thesis. The *XMM-Newton* observations of Aql X-1 are analyzed in chapters 3 and 4. Chapter 3 focuses on the broadband spectroscopy of Aql X-1 using the EPIC/pn

instrument on *XMM-Newton*, whereas chapter 4 is the analysis of the observations taken with the RGS instrument on *XMM-Newton* in order to look for emission lines from Aql X-1. In chapter 5 the *Chandra* observations are used in order to measure the radius of the neutron star in Aql X-1. The *XMM-Newton* and *Chandra* observations are both utilized in chapter 6 in a search for a candidate X-ray counterpart to a new population of neutron stars called RRATs. Finally, in chapter 7, the conclusions of the analysis of the previous chapters are summarized.

## CHAPTER 2 Satellites

### 2.1 Introduction

X-ray observations have revealed a universe of energetic phenomena. This is a different picture of the universe than in other wavebands. There are many classes of astrophysical objects which emit X-rays, including accreting neutron stars. Various telescopes have been built in order to understand the physical processes resulting in the high energy phenomena.

The X-ray sky was first comprehensively surveyed in 1970 with the *UHURU* satellite, which operated between the years of 1970-1973 (Giacconi et al., 1971). There have been many subsequent X-ray missions after *UHURU*. Table 2-1 is a list of the most prominent imaging X-ray satellites where observational capabilities of various observatories are compared. The sample of X-ray missions in the Table include *Einstein Observatory* (1978-1981), *ROSAT* (1990-1999), *ASCA* (1993-2001), *Chandra* and *XMM-Newton* (both 1999 to current).

The first fully imaging X-ray telescope was NASA's *Einstein Observatory*. The *Roentgen Satellite (ROSAT)* – a collaboration between Germany, the United Kingdom and the United States – spent the first six months of its nine years of operation dedicated to an all-sky survey which increased the number of cataloged X-ray sources from  $\sim 300$  to  $\sim 100\,000$ . The *Advanced Satellite for Cosmology and Astrophysics (ASCA)* was the first X-ray satellite to use CCD detectors which permitted modest

( $E/\Delta E=10$ ) X-ray spectral resolution. For this thesis work observations were taken with *XMM-Newton* and *Chandra*. These two X-ray satellites are described more completely below.

## 2.2 *XMM-Newton*

### 2.2.1 History and Telescope overview

The information on the *XMM-Newton* telescope, in the next three sections, is compiled from information in the Proposer's guide v.2.3, which can be found on the *XMM-Newton* website<sup>1</sup>. The European Space Agency's (ESA) *X-ray Multi-Mirror mission, XMM-Newton*, was launched on December 10, 1999. It carries X-ray and optical/UV telescopes for simultaneous observing over two wavebands. The characteristics of each of the telescopes of *XMM-Newton*, EPIC/MOS, EPIC/pn, RGS, and OM, are listed in Table 2-2. A schematic of the *XMM-Newton* is shown in Figure 2-1. There are two X-ray instruments: the European Photon Imaging Camera (EPIC) and the Reflection Grating Spectrometer (RGS). EPIC, used for spectro-imaging, is composed of three CCD cameras, two are Metal Oxide Semiconductor (MOS) cameras and the other is the pn camera. The RGS consists of 2 spectrometers that are used for high-resolution spectrometry. The optical/UV telescope is called the Optical Monitor (OM), this telescope is used for simultaneous optical and X-ray observations. There are three independent sets of focusing optics on *XMM-Newton*: one is in the front of the EPIC/pn camera; the other two focus

---

<sup>1</sup> [http://xmm.vilspa.esa.es/external/xmm\\_user\\_support/documentation/uhb/index.html](http://xmm.vilspa.esa.es/external/xmm_user_support/documentation/uhb/index.html)

Table 2–1: Overview of various X-Ray Telescopes

Satellite	Years of Operation	Spatial resolution (arcsec)	Energy Range	FOV (arcmin)	Spectral Resolution (E/ΔE)
<b>Einstein Observatory</b>	1978-1981	IPC: 60 HRI: 2	0.2-20keV	IPC: 75 HRI: 25	FPCS: 50-100 (E < 0.04keV) 100-1000 (E > 0.4keV)
<b>ROSAT</b>	1990-1999	HRI:2	0.1-2.5keV	PSPC:60 HRI:38	PSPC= $0.43(E/0.93)^{-0.5}$
<b>ASCA</b>	1993-2001	GIS: 30 SIS:30	0.4-10keV	GIS: 50 SIS:22	GIS: 8% at 5.9keV SIS: 2% at 5.9keV
<b>Chandra</b>	1999-current	<1	0.1-10keV	ACIS-I: 16 ACIS-S: 8×48 HRC: 30	ACIS (FI): 20-50 ACIS(BI): 9-35
<b>XMM-Newton</b>	1999-current	6	0.1-15keV	EPIC MOS: 33 EPIC pn: 27.5 RGS: 5	EPIC MOS: 20-50 EPIC pn: 20-50 RGS: 200-800

15

These are compiled from the HEASARC website: <http://heasarc.gsfs.nasa.gov/docs/corp/observatories.html>

ACIS: Advanced CCD Imaging Spectrometer

BI: Back Illuminated

EPIC: European Photon Imaging Camera

FI: Front Illuminated

FPCS: Focal Plane Crystal Spectrometer

GIS: Gas Imaging Spectrometer

HRC: High Resolution Camera

HRI: High Resolution Imager

IPC: Imaging Proportional Counter

MOS: Metal-Oxide Silicon PSPC: Position Sensitive Proportional Counter

RGS: Reflection Grating Spectrometer

SIS: Solid-State Imaging Spectrometer

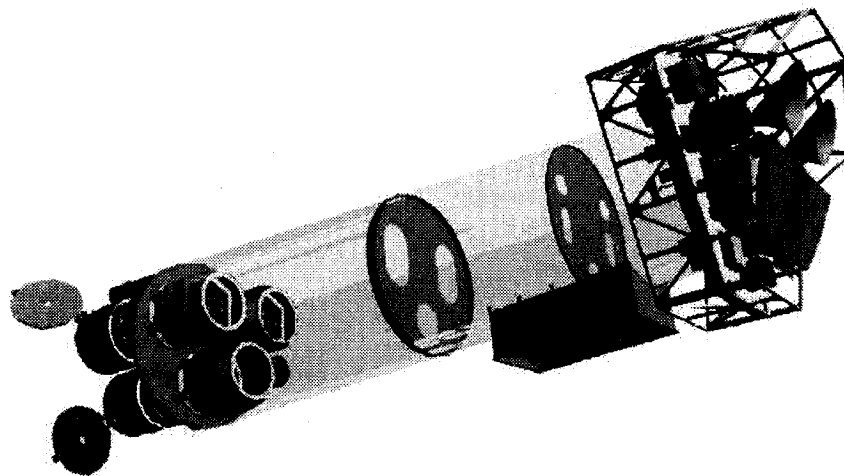


Figure 2–1: A schematic of the *XMM-Newton* satellite. At the lower left are three mirror modules, two of which are equipped with reflection grating arrays. At the right end are the X-ray instruments. Image is from the XMM proposer’s Guide v2.3 see website ([http://xmm.vilspa.esa.es/external/xmm\\_user\\_support/documentation/uhb/index.html](http://xmm.vilspa.esa.es/external/xmm_user_support/documentation/uhb/index.html)).

onto the EPIC/MOS camera. For the two telescopes focusing light onto the two EPIC/MOS detectors, only 44% reaches the EPIC/MOS detectors, while 58% is deflected and dispersed by the RGS assembly for high resolution spectroscopy.

### 2.2.2 Instruments

The *XMM-Newton* observations used in the analysis in this thesis work were collected from EPIC/pn and RGS. This section describes features of these two instruments.

Table 2-2: Overview of *XMM-Newton* Characteristics

Instrument	EPIC MOS	EPIC pn	RGS	OM
Bandpass	0.15-12keV	0.15-15keV	0.35-2.5 keV	180-600 nm
Orbital target vis.	5-135 ks	5-135 ks	5-135 ks	5-145 ks
Sensitivity <sup>(a)</sup>	$\sim 10^{-14}$ <sup>(b)</sup>	$\sim 10^{-14}$ <sup>(b)</sup>	$\sim 8 \times 10^{-5}$ <sup>(c)</sup>	20.7 mag <sup>(d)</sup>
Field of View (FOV)	30'	30'	$\sim 5$	17'
PSF(FWHM/HEW)	5"/14"	6"/15"	N/A	1.4"-2.0"
Pixel size	40 $\mu$ m (1.1")	150 $\mu$ m (4.1")	81 $\mu$ m ( $9 \times 10^{-3}$ Å)	0.476513"
Timing resolution	1.5 ms	73.4 ms <sup>(e)</sup>	16 ms	0.5 s
Spectral resolution	$\sim 70$ eV	$\sim 80$ eV	0.04/0.025 Å	350

This comparison of the different instruments of *XMM-Newton* is from the *XMM-Newton* Proposer's guide v2.3, see website ([http://xmm.vilspa.esa.es/external/xmm\\_user\\_support/documentation/uhb/index.html](http://xmm.vilspa.esa.es/external/xmm_user_support/documentation/uhb/index.html)).

a) After 10ks

b)  $\text{erg cm}^{-2} \text{s}^{-1}$ , 0.15-15.0keV

c)  $\text{photons cm}^{-2} \text{s}^{-1}$ , OVII 0.57keV line flux

d)  $5\sigma$  detection of an A0 star in 1000s

e) full window mode

## **EPIC/pn**

The EPIC/pn chip is composed of 12 CCDs which are integrated onto one silicon wafer. The CCDs are back-illuminated: X-rays hit the detector from the rear of the device. The timing resolution of the camera depends on the mode the observation is taken in. For an observation in timing mode the time resolution is 0.03ms and in burst mode the time resolution is 0.007ms. For the full window mode the time resolution is 73.4ms. All pn observations analyzed in this thesis were taken in full window timing mode. The energy resolution of the EPIC/pn is dependent on the photon energy. The energy resolution (FWHM) has a general trend of increasing the FWHM with increasing photon energy. The energy resolution also depends on if the photon events are doubles or singles and also how far from the readout mode the events occur. A single event is when only one pixel in a  $3\times 3$  pixel grid has an event. With doubles, there are photon events detected by the central pixel in the  $3\times 3$  grid and in a pixel adjacent to the central pixel. This energy dependence of the energy resolution of the EPIC/pn chip impacts the binning of the spectra extracted from EPIC/pn. As it is necessary to bin data such that the width of the bin is at-least as wide as the resolution, the spectral bin width changes with the energy of the photons.

## **RGS**

For high resolution X-ray spectroscopy *XMM-Newton* has the RGS. The RGS is suited for the energy range between 0.33-5.5keV. RGS has two units, RSG1 and RGS2, each of which are made of two components: the Reflection Grating Assembly (RGA) and the RGS Focal Cameras (RFCs). The RFCs are composed of nine back-illuminated (BI) MOS CCDs. Using BI CCDs maximizes the soft energy response.

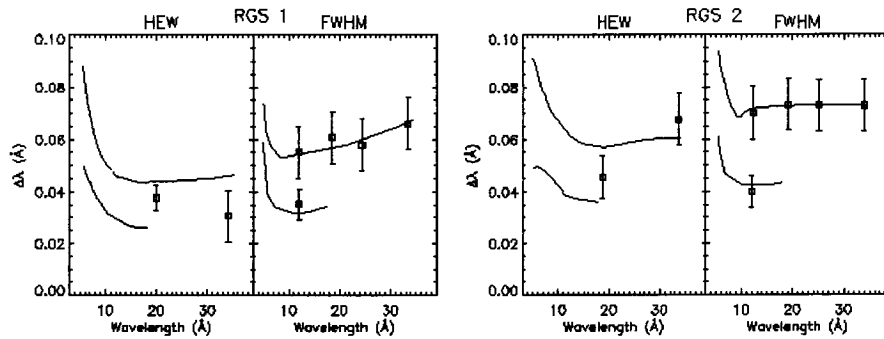


Figure 2-2: The energy resolution of the RGS units. The left Figure is the energy resolution of RGS1 with the HEW on the left and the FWHM on the right. The Figure on the right is the energy resolution of RGS2 with HEW on the left portion and FWHM on the right. The -1 and -2 grating orders for the RGS energy resolution are shown. Image is from the *XMM* proposer's Guide V2.3 see website ([http://xmm.vilspa.esa.es/external/xmm\\_user\\_support/documentation/uhb/index.html](http://xmm.vilspa.esa.es/external/xmm_user_support/documentation/uhb/index.html)).

There is an aluminum coating on the exposed sides of the RFCs in order to reduce optical and UV light from entering the RFC.

Of the nine CCDs on each of the RGS units, one has failed on each unit. On the RGS2, CCD4 ( $\lambda=20.0$  to  $24.1$  Å) failed after the first week of operation in December 1999. Then in September of 2000 CCD7 ( $\lambda=10.6$  to  $13.8$  Å) failed on RGS1. As a result there are gaps in the spectra from the RGS.

The resolving power of RGS1 and RGS2 differ. The resolving power of RGS1 and RGS2 in terms of half energy width (HEW) and full width at half maximum (FWHM) is displayed in Figure 2-2. The HEW is used for detection of weak features on the continuum, whereas the FWHM is used for closely spaced spectral lines.

### 2.2.3 *XMM-Newton* Data Preparation

The data preparation and analysis are performed using the Science Analysis Software (SAS) for *XMM-Newton* observations. The information compiled on the data preparation of EPIC/pn and RGS observations is from the SAS user guide v3.2<sup>2</sup>. The observation data files (ODF) include the raw event files from the three instruments: EPIC, RGS, and OM, as well as instrument files, files from the radiation monitor, and files which concern the functions of the spacecraft. There is a Pipeline Processing Subsystem (PPS) which generates data products. To prepare the observation data for analysis, a calibration index file (CIF) needs to be constructed. The CIF is made by running `cifcuild` which selects calibration files from the date of the observation; the CIF is specific to the ODF. A summary file is initially made with the PPS but needs to be extended with information from instrument housekeeping files. The summary file is extended using the SAS command `odfingest` which examines all the files including housekeeping and calibration files and then finally creating a new summary file. For each of the different cameras different tasks need to be performed in order to prepare the data for analysis. The following two sections cover the tasks required for data preparation for EPIC/pn and RGS.

#### **Data Preparation: EPIC/pn**

When the ODFs are received from *XMM-Newton* they have already been run through the pipeline and thus include calibrations. However, if there are improvements to the calibration files since receiving the ODF, the task `epproc` can be run

---

<sup>2</sup> see website: [http://xmm.vilspa.esa.es/external/xmm\\_sw\\_cal/sas\\_frame.shtml](http://xmm.vilspa.esa.es/external/xmm_sw_cal/sas_frame.shtml)

to reprocess the observations with current calibrations. The task **eproc** runs a sequence of five tasks: **epframes**, **badpixfind**, **badpix**, **epevents**, and **attcalc**. The task **epframes** creates a raw event list and good time interval (GTI) data set by processing the CCD, exposure and datamode that are specific to a an ODF. The task **badpixfind** finds new badpixels, then **badpix** processes the raw event list and to it adds a BADPIX extension list of badpixels. The task **epevents** processes the event list file and creates the calibrated event list and **attcalc** calculates the X and Y sky coordinates (X and Y offsets to a fixed position, used to convert CCD positions to absolute positions given in RA and DEC). After these five tasks are run, **eproc** runs the task **evlistcomb** which combines the data sets specific to a CCD to a single event list and then **evselect** is run to filter events, selecting events that arrive in GTIs.

#### **Data Preparation: RGS**

To prepare observations taken with RGS for analysis, the command **rgsproc** is run. It is an interactive version of the RGS pipeline. There are two parts to **rgsproc**: constructing a calibrated events list and selecting events used to create a spectrum. Running **rgsproc** with default settings produces 10 spectra: 5 for the first order spectra (2 RGS1, 2 RGS2 and a combined RGS1 and RGS2 spectrum) and similarly for the second order. In this thesis only the first-order is analyzed. In the default setting of **rgsproc** there are five processing stages of the data: events, angles, filter, spectra and fluxing. In the events stage the preliminary tasks are performed as well as some source independent calibrations. In the second stage of **rgsproc**, angles, the source coordinates are corrected for aspect drift. Next in the filter stage, a filtered

event list is produced keeping events with Time-of Arrivals (TOAs) within the range specified in the good time interval (GTI) tables. The fourth stage, spectra, involves creating the spectra for each of the sources, a source list is also created which lists the sources and the order. In the final and fifth stage, fluxing, a fluxed spectrum is created of the primary source as well as response matrices. The fluxed spectrum is a combination of RGS1 and RGS2 flux calibrated spectra using the effective area calculated from the response matrix. After `rgsproc` is run for the first time it can be run again in order to filter out times of high background count rates or to bin the data for analysis.

## 2.3 *Chandra*

### 2.3.1 History and Telescope overview

The information on the *Chandra* satellite is compiled from the *Chandra* Proposer's Guide v.8 <sup>3</sup>. *Chandra* was launched on July 23, 1999 and is one of NASA's four great observatories. These four observatories include the *Hubble Space Telescope*, the *Compton Gamma-Ray observatory*, and the *Spitzer Space Telescope*. A schematic of the the *Chandra* observatory is shown in Figure 2-3. The *Chandra* telescope has two main science instruments: the Advanced CCD Imaging Spectrometer (ACIS) and the High Resolution Camera (HRC). *Chandra* also has two objective transmission gratings, the High Energy Transmission Grating (HETG) and the Low Energy Transmission Grating (LETG). The observations used in the thesis were taken with ACIS, discussed below.

---

<sup>3</sup> see webpage: <http://cxc.harvard.edu/proposer/POG/html/>

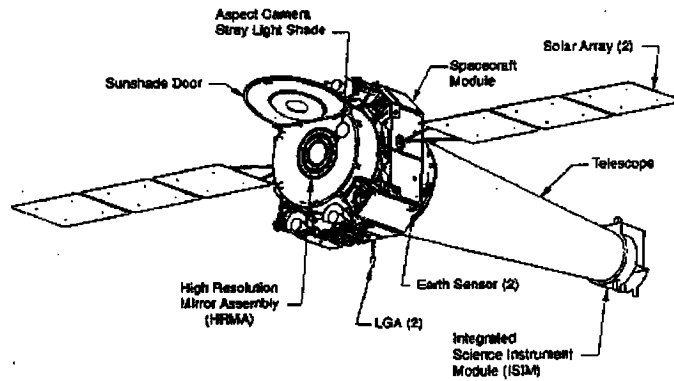


Figure 2-3: A schematic of the *Chandra* observatory. The systems on the telescope are labeled. Image from the *Chandra* Proposer's Guide, see website (<http://cxc.harvard.edu/proposer/POG/html/>).

### 2.3.2 Instruments

The ACIS was developed in a collaboration between Penn State, MIT Center for Space research and the Jet Propulsion Lab. The CCDs that are used in ACIS were developed by MIT. To stop optical photons from entering the camera, optical filters are placed over the CCDs. These optical filters are composed of a polycarbonate plastic which is sandwiched between two layers of aluminum.

ACIS is composed of ten CCDs (Figure 2-4). There are two components to ACIS: ACIS-I and ACIS-S. ACIS-I is used for imaging and uses four of the CCDs. The six other CCDs are ACIS-S and are used either for imaging or as a grating readout. Of the ten CCDs, two are BI (S1 and S3) with the remaining eight FI. The BI CCDs are more sensitive to low energies than the FI and have better energy resolution compared to the FI. However, since launch, the sensitivity of the BI CCDs have degraded – it is thought to be due to the collection of exhaust from the satellite attitude system on the CCD surface – such that the response of the BI CCDs below

## ACIS FLIGHT FOCAL PLANE

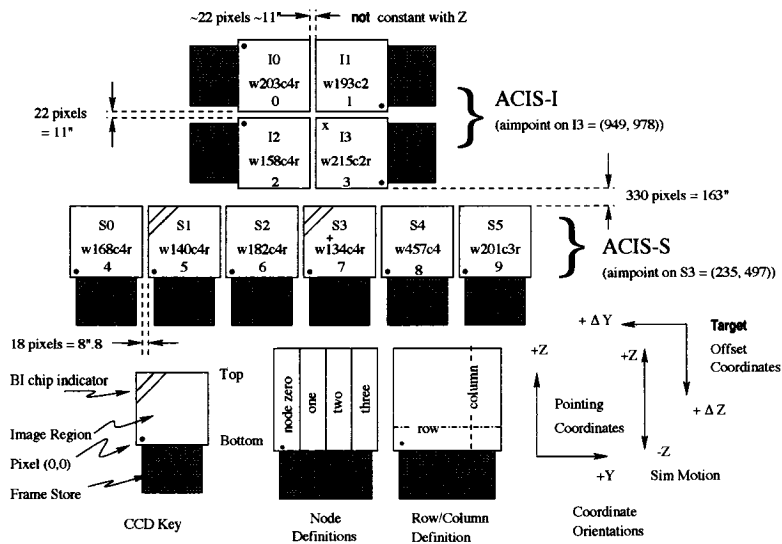


Figure 2-4: The focal plane of ACIS. The CCD ACIS-S3 was the one used for the observations. ACIS-S3 is a back illuminated CCD. Image from the *Chandra* Proposer's Guide, see website (<http://cxc.harvard.edu/proposer/POG/html/>).

1keV is now comparable to that of the FI CCDs. The pre-launch energy resolution of ACIS is displayed in Figure 2-5. Before launch the FI CCDs had better energy resolution than the BI, but due to damage sustained by ACIS during flight, the energy resolution of the FI has depleted, but the BI energy resolution is unchanged.

### 2.3.3 Data Preparation

The information on the data preparation of *Chandra* observations can be found on the *Chandra* X-ray Center website.<sup>4</sup> The observation files from *Chandra* are

<sup>4</sup> <http://cxc.harvard.edu>

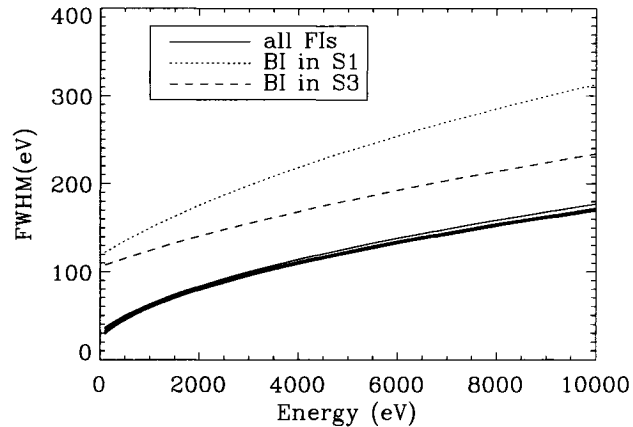


Figure 2-5: The energy resolution of ACIS before launch. The dashed curve represents the resolution of ACIS-S3. After launch the resolution of the FI CCDs degraded. Image from the *Chandra* Proposer's Guide, see website (<http://cxc.harvard.edu/proposer/POG/html/>).

processed through a pipeline. There are three levels to the data processing through the pipeline:

**Level 0 (L0):** the raw spacecraft telemetry is split into files, then the telemetry is divided along the boundaries of the observation. This level is not used at the level of the user analysis.

**Level 1 (L1):** starting with the output from the L0, corrections that are instrument independent, such as the aspect solution, are applied. There is nothing irreversible done to the observation data at L1, such as photon rejection. It is from these event files that reprocessing of *Chandra* observations are started.

**Level 2 (L2):** The output of L1 has corrections applied such as filtering for good time intervals, rejecting cosmic rays, and transforming the position to celestial coordinates. These corrections are standard, but also irreversible.

The analysis of *Chandra* observations can be started with the event files output from L2. However, if there have been improvements to the calibration files or the analysis software (CIAO), the observations can be reprocessed from the L1 event files to create new L2 event files.

The steps for making a new L2 event file from the L1 event file include improving the astrometry of the data and removing flags of possible cosmic ray events in the L1 file. These cosmic ray event flags are removed because a new method of identifying afterglow events (excess charge) was introduced in later versions of CIAO. Using the latest method, hot pixels and cosmic ray afterglow events are flagged. A new bad pixel file is created for the observation. Then, filtering the L1 event file for bad grades and good time intervals results in the new L2 event file. This new L2 event file can then be used for calibrated data analysis.

#### **2.4 *RXTE* All-Sky Monitor**

The All Sky Monitor (ASM) is on the *Rossi X-ray Timing Explorer (RXTE)* and has been monitoring the sky since February of 1996 in the 1.5-12keV band. There are three cameras which make up the ASM. These are free to rotate to view different regions of the sky. The sky is observed in a highly variable fashion with randomly selected sources being scanned five-ten times in a day. The transient sources in the sky are often below the threshold of ASM detection, but could be detected when bright. All the intensities of the objects observed with ASM are corrected with

respect to observations of the Crab nebula (Levine et al., 1996). The observation data from ASM is available from the MIT RXTE website.<sup>5</sup>

## 2.5 Summary

To expand knowledge of neutron stars or other high energy emitting phenomena, observations in the X-ray band can be utilized. To this end X-ray observations have been taken of Aql X-1. Observations of Aql X-1 at low flux allow one to make radius measurements and study low flux behavior. To observe Aql X-1 in a low flux state EPIC/pn on *XMM-Newton* and ACIS-S on *Chandra* are used. In the *XMM-Newton* observations Aql X-1 was caught in a state of active accretion, using EPIC/pn this state can be characterized. Also, with Aql X-1 in this state of active accretion the RGS spectra is summarily examined to search for low equivalent width absorption and emission lines. This analysis is performed since RGS on *XMM-Newton* has the capability to make the type of observations that can be used to search for spectral lines. The ACIS instrument on *Chandra* is useful for high resolution imaging with moderate spectral resolution of faint sources ( $\sim 10^{-13}$  erg cm<sup>-2</sup> s<sup>-1</sup>). Observations of Aql X-1 in quiescence with ACIS-S on *Chandra* make it possible to measure the radius of Aql X-1 and investigate variability in Aql X-1 from observation to observation. The ASM on *RXTE* monitors the entire sky and can detect Aql X-1 when in outburst, which puts the *XMM-Newton* and *Chandra* observation in context with Aql X-1 in outburst.

---

<sup>5</sup> <http://xte.mit.edu>

## CHAPTER 3

### *XMM-Newton* Observations of Aql X-1

#### 3.1 Introduction

Aql X-1 is a soft X-ray transient (SXT) low mass X-ray binary (LMXB) with an  $\sim$  yearly outburst recurrence (Priedhorsky & Terrell, 1984). Aql X-1 has been observed in quiescence with a luminosity of  $\sim 10^{33}$  ergs $^{-1}$  (Verbunt et al., 1994; Asai et al., 1998; Campana et al., 1998; van Paradijs et al., 1987; Rutledge et al., 2001a). Since Aql X-1 returns to this quiescent luminosity repeatedly after different outbursts, this indicates a mechanism which establishes this luminosity. It has been proposed that “deep crustal heating” is the mechanism responsible for continually re-establishing the quiescent luminosity (Brown et al., 1998). With deep crustal heating the quiescent luminosity is due to a hot core. For more details on deep crustal heating see Chapter 1.

However, observations of quiescent low mass X-ray binaries (qLMXBs), at luminosity's of  $\sim 10^{33}$  ergs $^{-1}$  have shown that there can be variability in the luminosity on the timescale of minutes (Campana et al., 2004, Cen X-4), days (Campana et al., 1997, Cen X-4), to weeks (Rutledge et al., 2001a, Aql X-1) to years (Rutledge et al., 2001b, Cen X-4). The deep crustal heating would establish a base luminosity, but it does not explain the observed X-ray variability. A small perturbation in the temperature of the crust of a system with an  $\sim 1$  month long outburst to variability timescale expected with deep crustal heating is from weeks to months, not minutes

to days (Ushomirsky & Rutledge, 2001). The timescales at which the variability occurs suggests the variability could be due to accretion processes occurring when the LMXB is in quiescence. Little is known about what governs the accretion rate in transient systems at low luminosities.

Observations of Aql X-1 were taken with *XMM-Newton* to study the variability while in quiescence. However, the source in the *XMM-Newton* observations was observed with luminosities of  $\sim 10^{36}$  erg s $^{-1}$ —  $\sim$ three orders of magnitude above the quiescent luminosity. This luminosity is between an outburst luminosity and a quiescent luminosity. The two *XMM-Newton* observations were analyzed and compared to the 11 *Chandra* observations and *All Sky Monitor* observations of Aql X-1.

### 3.1.1 Global Lightcurve of Aql X-1

Figure 3-1 compares the two *XMM-Newton* and 11 *Chandra* observations to  $\sim$ 4 years of observations of Aql X-1 taken with the ASM on *RXTE* from October of 2000 to January of 2005. The ASM observations are able to monitor Aql X-1 during times of outburst. The *Chandra* observations caught Aql X-1 during quiescence ( $L_x \sim 10^{33}$  erg s $^{-1}$ ). The luminosities of the *Chandra* observations are calculated, using an absorbed hydrogen atmosphere, in section 5.5.1. The luminosities of the *XMM-Newton* observations are calculated in this chapter in section 3.4. The two *XMM-Newton* observations, compared to the ASM and *Chandra* observations, indicate Aql X-1 was at an intermediate luminosity during the observations indicating the luminosity is dominated by continued disk accretion, rather than thermal atmospheric emission, as required for measuring the neutron star radius using a hydrogen

Table 3–1: All *XMM-Newton* and *Chandra* observations of Aql X-1 used in thesis

ID	Start Time (TT)	GTI (sec)	Observatory/Instrument
708	2000 Nov 28 10:52:39	6628	<i>Chandra</i> /ACIS-S
709	2001 Feb 19 11:25:52	7787	<i>Chandra</i> /ACIS-S
710	2001 Mar 23 20:09:11	7390	<i>Chandra</i> /ACIS-S
711	2001 Apr 20 11:53:32	9245	<i>Chandra</i> /ACIS-S
3484	2002 May 4 22:43:16	6494	<i>Chandra</i> /ACIS-S
3485	2002 May 20 07:22:31	6958	<i>Chandra</i> /ACIS-S
3486	2002 Jun 11 03:32:05	6486	<i>Chandra</i> /ACIS-S
3487	2002 Jul 5 15:28:48	5940	<i>Chandra</i> /ACIS-S
3488	2002 Jul 22 20:45:10	6505	<i>Chandra</i> /ACIS-S
3489	2002 Aug 18 07:57:08	7128	<i>Chandra</i> /ACIS-S
3490	2002 Sep 3 16:08:35	6936	<i>Chandra</i> /ACIS-S
XMM-1	2004 Apr 13 18:30:16	3419	<i>XMM</i> /EPIC and RGS
XMM-2	2004 Apr 19 13:36:20	18837	<i>XMM</i> /EPIC and RGS

atmosphere. Nonetheless, we perform a basic spectral analysis to describe Aql X-1’s state, including a search for spectral lines.

### 3.2 Observations and Data Reduction

All the observations used in this thesis are described in Table 3–1. For the *XMM-Newton* observations, SAS v6.0.0 and XSPEC v11.3.1 were used for data analysis and spectral fitting. The *XMM-Newton* observations of Aql X-1 were put into context with the 11 *Chandra* observations listed in Table 3–1. The analysis software CIAO v3.3 and CALDB v3.2.1 were utilized for the analysis of *Chandra* observations.

Both of the *XMM-Newton* observations were taken in imaging mode with a full window and thin filter. For XMM-1 the time from beginning of the exposure to the end of the exposure was 8ks, but the live time of the observation was only 3.4ks. Similarly for XMM-2 an observation that had start to end exposure time of 21ks, due to live time the observation time decreased to 19ks. Then, with filtering (see

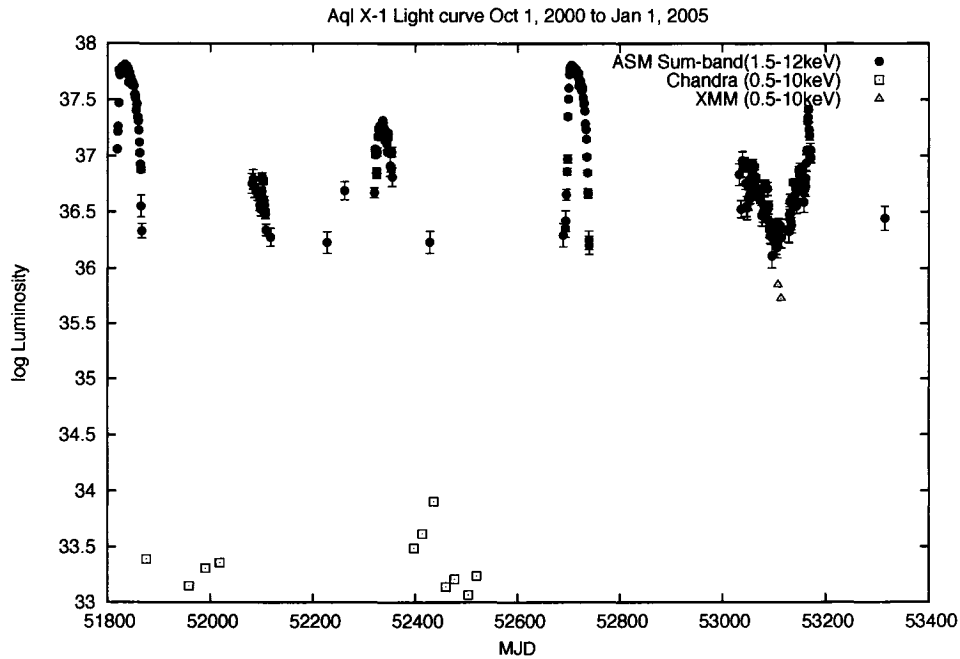


Figure 3-1: Putting the XMM-Newton observations into context. The filled circles are from the All Sky Monitor, where only those observations by ASM that were above a  $4\sigma$  detection were used. The squares are the 11 Chandra observations and the triangles are the two XMM-Newton observations. The Chandra measurements are from the spectral fits in Chapter 5. The ASM count rates were converted to flux by assuming  $1\text{ASM count/s} = 4.4 \times 10^{-10} \text{ erg cm}^{-2} \text{ s}^{-1}$  (0.5-10.0keV; for a  $kT=5\text{keV}$  thermal bremsstrahlung spectrum corrected for absorption). The error bars for both the Chandra and the XMM-Newton observations are smaller than the data points and have not been included in the plot. The XMM-Newton observations are above a level of quiescence, where the Chandra observations lie, yet below outburst luminosities, where the ASM observations lie.

next section) XMM-2 for good time intervals (GTIs) the observation time further decreased to 16ks. The *Chandra* observations were all taken on the CCD ACIS-S3. The observations 708, 709, 710, and 711 were taken in VFAINT mode. The other *Chandra* observations: 3484, 3485, 3486, 3487, 3488, 3489, and 3490, were taken in FAINT mode.

Calibration files were created for the *XMM-Newton* observations using the command `cifbuild`. The calibration files are specific to the date of the original observation and to the data of the analysis. A summary file of the observation data files (ODF) was made with the SAS command `odfingest`. The summary file is required for the reduction meta-task `eprocc` which process the data. Calling on the task `eprocc` calls on other tasks which create an event list and a good time interval data set, locate and flag badpixels, creates a calibrated event list, calculates the X and Y coordinates and combines the data sets from specific CCDs to a single event file.

### 3.3 Statistical Methods

The statistical methods employed in fitting models to the observations are described in depth within Bevington & Robinson (2003), here we give a brief overview. To begin, the errors on the observation data points are assumed to be Gaussian for the fitting process. The deviation of the model and the observation data points is indicated by  $\chi^2$ . The process of fitting the model to the observation involves many iterations of the model in order to minimize the  $\chi^2$ . Between iterations the model parameters are increased or decreased. The method used in XSPEC to minimize

$\chi^2$  is based on the Levenberg-Marquardt algorithm<sup>1</sup>. Once a minimized  $\chi^2$  is found, whether or not the model is statistically acceptable fit is indicated by the  $\chi^2_\nu$ . A  $\chi^2_\nu$  much greater than 1 or a very small  $\chi^2_\nu$  are both statistically unacceptable and the model is not appropriate for the observations. The parameters of the model have associated errors, the errors of the model parameters throughout this thesis are to the 90% confidence level, unless otherwise noted. This 90% confidence level on the errors means a random measurement would have a 90% probability of falling within 2.706 standard deviations ( $2.706\sigma$ ) of the mean.

### 3.4 Analysis

Of the 13 observations of Aql X-1 listed in Table 3-1, two were taken with *XMM-Newton*. For both of the observations source counts were extracted from a circular region centered at the coordinates of Aql X-1 with a radius of 28". The background counts were taken from a larger circular region of 120" radius from a region far from Aql X-1, but still on the same CCD chip.

The *XMM-Newton* observations were checked for times of background flaring, this is displayed Figures 3-2 and 3-3, for XMM-1 and XMM-2, respectively. The Figure 3-2 for XMM-1 shows that there were many times of high background, as a result, the observation was not filtered for the analysis. The average count rate for the source region in XMM-1 is  $42.8 \pm 0.1$  counts/s and a count rate of 10 counts/s in the background region corresponds to 0.5 counts/s in the source region. The background counts account for  $\sim 1\%$  of the counts in the source region of XMM-1. In Figure 3-3,

---

<sup>1</sup> <http://heasarc.gsfc.nasa.gov/docs/xanadu/xspec/manual/manual.html>

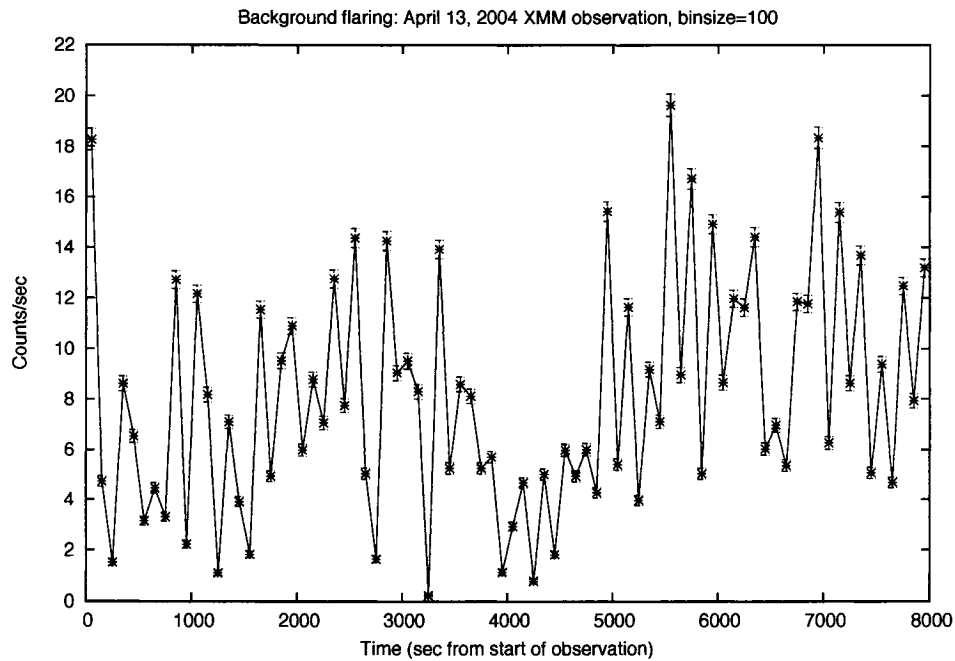


Figure 3-2: Looking for background flaring in XMM-1 by taking a lightcurve of the whole chip and seeing if there are times when there are excess counts. Since the whole observation has a high background there was not any filtering of the data performed. A count rate of 10 c/s in the background region is equal to 0.5c/s in the source region, as compared with the average source count rate of  $42.8 \pm 0.1$  c/s. The background does not dominate the source counts.

for XMM-2, there are distinct times of flaring. Filtering the observation such that times where the count rate was above 1 count/s were excluded results in a source count rate of  $28.80 \pm 0.04$  counts/s. A count rate of 1 count/s in the background is equal to 0.05 counts/s in the source region,  $\sim 0.2\%$  of the source counts. Since the background only contributes a count rate of 0.2% to the source and there is no significant impact on the spectral fits of XMM-2, the unfiltered XMM-2 observation was used for the analysis. For both XMM-Newton observations the background does not greatly affect the source region.

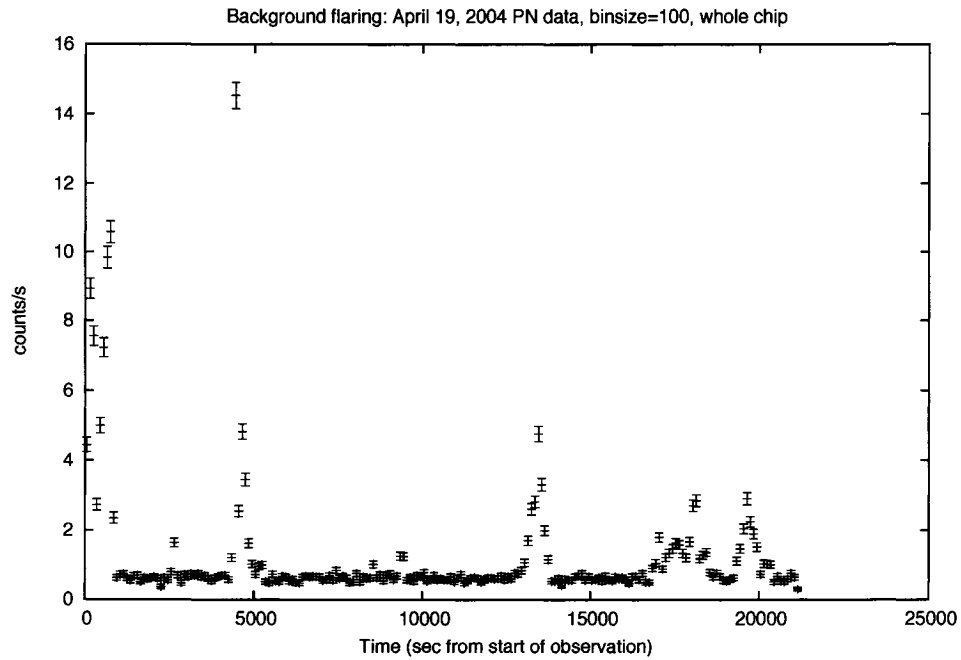


Figure 3-3: Looking for background flaring in XMM-2 by taking a lightcurve of the whole chip. A count rate of 1c/s in the background region is equal to 0.05c/s in the source region, as compared to the average count source count rate in a filtered observation of  $28.80 \pm 0.04$  c/s. The unfiltered observation was used for spectral analysis.

Using the previously defined regions for the source and the background, lightcurves were constructed for the two XMM-Newton observations using the unfiltered data. Due to time in the XMM-Newton observations being lost due to live time, lightcurves could not be constructed by simply binning the count rate at every 1000s, this would underestimate the count rate. Instead, at every 1000 second interval of the observation, from the start of the first event recorded to the last, a spectrum was extracted to determine the number of counts. The counts were then divided by the actual live time during the 1000s interval. The lightcurve of Aql X-1 in XMM-1 with the background subtracted is shown in Figure 3-4. The lightcurve of Aql X-1 from XMM-2 of the unfiltered observation without the background subtracted is shown in Figure 3-5. Both light curves display a variability of no more than a few percent.

A source and background spectrum were extracted from both XMM-1 and XMM-2. The background spectrum was subtracted from the source during spectral fitting. The extracted spectra was binned according to the resolution of the chip, where the minimum bin-width is given by (Rutledge & Sako, 2003):

$$FWHM(E) = 57 + 13(E/1\text{keV}) - 0.29(E/1\text{keV})^2\text{eV} \quad (3.1)$$

where the bin-size is determined from the full width at half maximum (FWHM). For the energies below 2keV each bin was 160eV wide, for energies between 2 and 4 keV the bins were 410eV wide and energies greater then 4keV the bin width was 2750eV wide. For energies below 0.2keV and above 10keV the counts were ignored. Each of the spectra were fit to an absorbed hydrogen atmosphere model plus power-law,

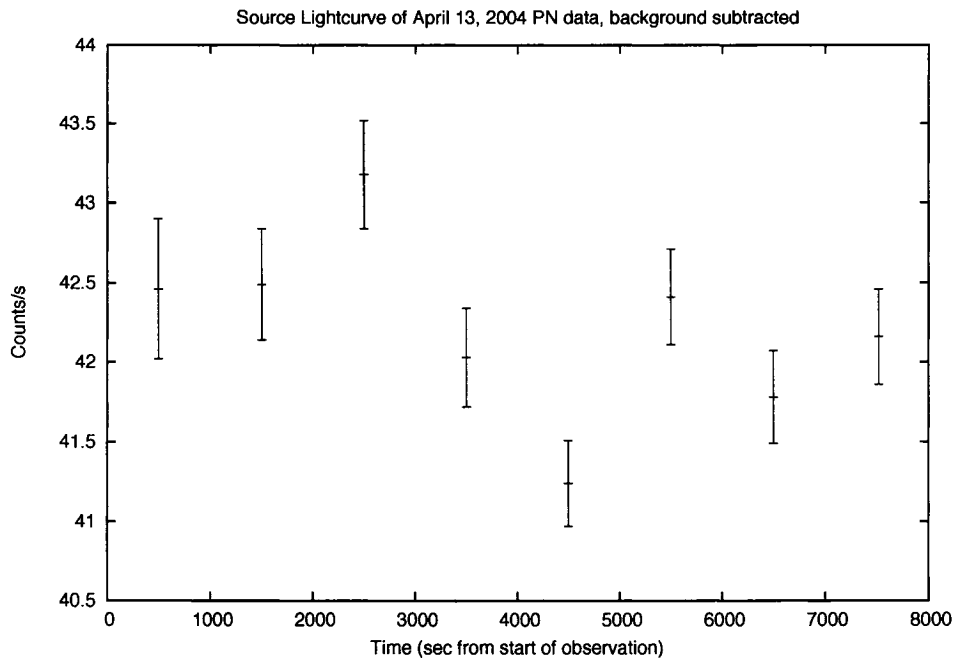


Figure 3-4: Lightcurve of the April 13, 2004 observation with the background subtracted from the source. The source was centered at the coordinates of Aql X-1 with a circle of radius  $28''$  and the background was taken from a region far from the source but still on the same CCD chip as Aql X-1 using a circular region of radius  $120''$ . The count rates for both the source and the background take into account the live time of the observation.

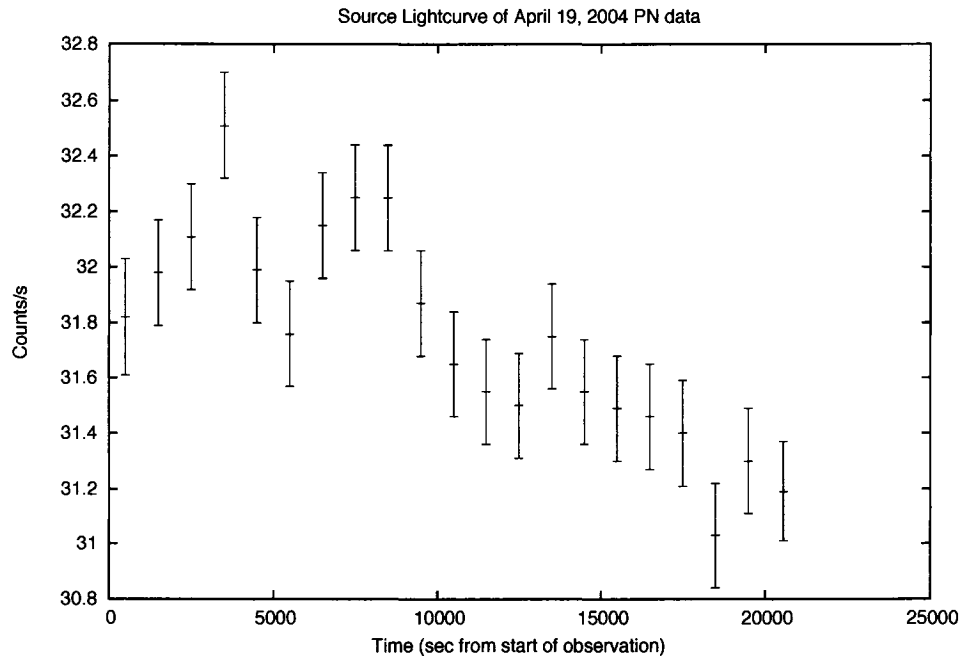


Figure 3-5: April 19, 2004 observation: source lightcurve of the unfiltered observation without the background subtracted. The counts were extracted from a circular region of a 28" radius centered on Aql X-1. The count rates take into account the live time of the observation.

an absorbed power-law, an absorbed black body plus power-law, an absorbed disk blackbody, and an absorbed disk black body plus power-law.

### 3.5 Results

The parameter fits to the background subtracted source spectra extracted from XMM-1 and XMM-2 are listed in Tables 3-2 and 3-3. Complete descriptions of each of the spectral models can be found on the XSPEC website.<sup>2</sup> The absorption model in XSPEC used was **wabs**, which has only one parameter, the equivalent of the hydrogen column. The hydrogen atmosphere model, **nsa** (Zavlin et al., 1996), describes a hydrogen atmosphere of the neutron star. The parameters of the model include the effective temperature, mass, radius, magnetic field strength and distance to the neutron star. The power law model fits to the index of the power law and the photons/keV/cm<sup>2</sup>/s at 1keV. The spectral model of a blackbody fits for a temperature and luminosity. The disk blackbody model is for a spectrum which arises from continuous variation of temperature in an optically thick accretion disk. The disk blackbody model fits for the temperature at the inner disk and also on the parameter:  $((R_{in}/\text{km})/(D/10\text{kpc}))^2 \cos \theta$ , where  $R_{in}$  is the inner disk radius,  $D$  is the distance to the source and  $\theta$  is the angle of the disk normal, relative to the line of sight. For all the spectral fits the absorption and the power law components were allowed to vary. For XMM-1 a spectral fit of an absorbed disk blackbody with a power law was not performed since just an absorbed disk blackbody gives a statistically acceptable fit

---

<sup>2</sup> <http://heasarc.gsfc.nasa.gov/docs/xanadu/xspec/xspec11/manual/manual.html>

( $\chi^2_{\nu} / \text{dof} = 1.97/15$ , prob.=0.01). Whereas, XMM-2 is best described by an absorbed disk blackbody with a power-law ( $\chi^2_{\nu} / \text{dof} = 0.47/15$ , prob.=0.94).

The fluxes of all the observations indicate that the luminosity of Aql X-1 during this time is  $\sim 10^{36} \text{ erg s}^{-1}$ , which is three orders of magnitude higher than the quiescent luminosity. Aql X-1 was not in quiescence during the *XMM-Newton* observations and therefore cannot be used for radius measurements using the hydrogen atmosphere model.

### 3.6 Discussion and Conclusions

The spectral fits of the two *XMM-Newton* observations of Aql X-1 were best described by an absorbed disk blackbody model for XMM-1 and an absorbed disk blackbody with a powerlaw for XMM-2. From the spectral fits of XMM-1 and XMM-2 the luminosity of Aql X-1 was found to be  $\sim 10^{36} \text{ erg s}^{-1}$ . Comparing this luminosity to the quiescent and outbursting luminosities of Aql X-1, as seen in Figure 3-1, indicates Aql X-1 was at an intermediate luminosity. Other observations of Aql X-1 were reported close to the time of the two *XMM-Newton* observations. Before the two *XMM-Newton* observations were taken, an optical outburst for Aql X-1 was reported on March 27, 2004, where the optical counterpart to Aql X-1 was observed to have a flux comparable to the 1996 mini-outburst of Aql X-1 (Ilovaisky & Chevalier, 2004). After the *XMM-Newton* observations on May 18, 2004, Aql X-1 was reported to have a detection with *INTEGRAL* where Aql X-1 was emitting hard X-rays between May 13 and 15, 2004. This detection would suggest that Aql X-1 was, in May 2004, entering a stage of outburst (Rodriguez et al., 2004). This observation indicates that a month after the two *XMM-Newton* observations, Aql X-1 was perhaps moving

Table 3-2: Spectral Fits of Aql X-1 from the two *XMM-Newton* observations

Parameter	XMM-1	XMM-2
net count rate	42.8±0.1	32.14±0.04
Absorbed Hydrogen atmosphere with a power-law		
$N_{H,22}^a$	0.236 $^{+0}_{-0.002}$	0.344 $^{+0.000}_{-0.001}$
Log $T_{eff}$ (K)	5.11±0.01	5.438 $^{+0.002}_{-0.015}$
$R_\infty^b$	20.50 $^{+0.13}_{-0.03}$	12.0 $^{+0.2}_{-0.0}$
$\alpha$	1.37 $^{+0.00}_{-0.01}$	1.612 $^{+0.000}_{-0.003}$
$N_{PL}^c$	3.00 $^{+0.10}_{-0.04} \times 10^{-2}$	3.05 $^{+0.06}_{-0.05} \times 10^{-2}$
Flux $^d$	2.77	2.12
$\chi_\nu^2$ (prob)	7.30/13(1.58×10 $^{-14}$ )	4.44/13(1.35×10 $^{-7}$ )
Absorbed power-law		
$N_{H,22}^a$	0.238 $^{+0.000}_{-0.002}$	0.334 $^{+0.000}_{-0.001}$
$\alpha$	1.35±0.01	1.571 $^{+0.002}_{-0.000}$
$N_{PL}^c$	2.99 $^{+0.04}_{-0.06} \times 10^{-2}$	2.94 $^{+0.08}_{-0.05} \times 10^{-2}$
Flux $^d$	2.84	2.12
$\chi_\nu^2$ (prob)	6.24/15(2.08×10 $^{-13}$ )	3.70/15(1.46×10 $^{-6}$ )
Absorbed Blackbody with a power-law		
$N_{H,22}^a$	0.44 $^{+0.02}_{-0.09}$	0.52±0.05
kT(keV)	0.083 $^{+0.002}_{-0.011}$	0.087 $^{+0.003}_{-0.006}$
$N_{BB}^e$	3.7 $^{+3.0}_{-0.2} \times 10^{-2}$	2.9 $^{+2.4}_{-1.1} \times 10^{-3}$
$\alpha$	1.54 $^{+0.02}_{-0.06}$	1.72 $^{+0.06}_{-0.03}$
$N_{PL}^c$	3.9 $^{+0.2}_{-0.3} \times 10^{-2}$	3.7 $^{+0.3}_{-0.1} \times 10^{-2}$
Flux $^d$	3.34	2.67
$\chi_\nu^2$ (prob)	4.13/13(6.76×10 $^{-7}$ )	2.17/13(8.31×10 $^{-3}$ )

All errors are to 90% confidence.

$a$ : cm $^{-2}$

$b$ :  $R_\infty=R_*/g_r$

$c$ : photons cm $^{-2}$ s $^{-1}$ at1keV

$d$ : unabsorbed flux, ×10 $^{-10}$  erg s $^{-1}$  (0.5-10.0keV)

$e$ :  $L_{39}/(D/10\text{kpc})^2$

Table 3–3: Spectral Fits of Aql X-1 from the two *XMM-Newton* observations continued

Parameter	XMM-1	XMM-2
net count rate	42.8±0.1	32.14±0.04
Absorbed Disk Blackbody		
$N_{H,22}^a$	0.126 $^{+0.008}_{-0.005}$	0.187 $^{+0.001}_{-0.000}$
$T_{in}(keV)$	2.5±0.1	2.004 $^{+0.004}_{-0.000}$
$N_{DBB}^e$	0.33 $^{+0.04}_{-0.01}$	0.58±0.01
Flux <sup>c</sup>	2.44	1.80
$\chi^2_{\nu}$ (prob)	1.97/15(0.01)	6.58/15(2.34×10 <sup>-14</sup> )
Absorbed Disk Blackbody with a powerlaw		
$N_{H,22}^a$	...	0.21±0.01
$T_{in}(keV)$	...	1.6 $^{+0.1}_{-0.3}$
$N_{DBB}^e$	...	1.2 $^{+0.6}_{-0.3}$
$\alpha$	...	-1.9 $^{+3.1}_{-1.1}$
$N_{PL}^b$	...	1.3 $^{+26.5}_{-1.0}$ ×10 <sup>-5</sup>
Flux <sup>c</sup>	...	1.88
$\chi^2_{\nu}$ (prob)	...	0.47/15(0.94)

All errors are to 90% confidence.

<sup>a</sup>: cm<sup>-2</sup>

<sup>b</sup>: photons cm<sup>-2</sup>s<sup>-1</sup> at 1keV

<sup>c</sup>: unabsorbed flux, ×10<sup>-10</sup> erg s<sup>-1</sup> (0.5-10.0keV)

<sup>d</sup>:  $L_{39}/D_{10}^2$

<sup>e</sup>:  $((R_{in}/km)/(D/10kpc))^2 \cos \theta$

into an outburst phase in which the accretion rate would increase. The observations of Aql X-1 on April 13 and 19, 2004 with the reports of activity before and after the observations indicate that Aql X-1 could not be in quiescence and was accreting at too high of a rate for the source to be in quiescence but also accreting at a rate that is less than for an outburst.

## CHAPTER 4

### High Resolution Spectroscopy

#### 4.1 Introduction

The high resolution spectroscopy available with the Reflection Grating Spectrometer (RGS) (den Herder et al., 2001) on *XMM-Newton* makes it possible to search for X-ray spectral lines. The spectral line features in RGS observations can indicate the type of companion a neutron star has in an LMXB by calculation the abundances of elements indicated by spectral features (Juett & Chakrabarty, 2003). This type of analysis of the RGS observation of Aql X-1 is not immediately important as the spectral type of the companion in Aql X-1 is not in doubt. Identified emission lines can also provide a measure of the gravitational redshift close to the neutron star surface or be interpreted as an indication of moving plasma, such as a jet (Tiengo et al., 2005). Absorption lines detected in an X-ray burst with RGS provided a measure of the gravitational redshift in the photosphere of the neutron star EXO0748-676. The measured gravitational redshift indicated a mass-to-radius ratio. Assuming a range of mass values, the mass-to-radius ratio can put constraints on the dense matter equation of state for the specified mass range (Cottam et al., 2002). Identified spectral lines have the possibility of containing information about the neutron star companion, the presence of jets or the gravitational redshift near the surface of the neutron star.

The fluxes measured in chapter 3 of the *XMM-Newton* EPIC/pn observations indicate that Aql X-1 was not in quiescence during the two observations; as a result there is a possibility that spectral lines may be present. Where chapter 3 focused on the broadband spectroscopy of Aql X-1 using EPIC/pn, here a search for spectral lines is conducted using the RGS instrument on *XMM-Newton*.

## 4.2 Observations and data reduction

The two observations taken with RGS are described in Table 3–1. For analysis of *XMM-Newton* RGS data, SAS v6.0.0 and XSPEC v11.3.1 were used. The incoming photons to RGS are dispersed as shown in Figure 4–1. The observational data was reduced using the SAS command `rgsproc` as described in Chapter 2. After this initial processing a lightcurve was made of the background of the CCD number 9 chip (CCD9). The CCD9 is closest to the optical axis of the telescope and is thusly most affected by background flaring. Figure 4–2 is a lightcurve of the CCD9 from XMM-1 observation with both the RGS1 and RGS2 plotted. The SAS User’s Guide<sup>1</sup> outlines a strategy for assesing the background in RGS: in general, count rates above 1 count/s on CCD9 are considered suspect. For both RGS observations a count rate of 1 count/s on CCD9 was used to in order to distinguish good time intervals (GTIs) of the observations, the times with a count rate below 1 count/s. The times where the count rate was below 1 count/s were stored in a GTI table. The channels were rebinned such that each bin was not wider than the resolution of the RGS at 2keV. Since RGS is not calibrated above 1.9keV, the resolution at 2keV gives the maximum

---

<sup>1</sup> see: <http://xmm.vilspa.esa.es/sas/new/documentation/>



Figure 4-1: The lower Figure illustrates the dispersion of the incoming photons on RGS1. The angle of dispersion is along the x-axis with the PI(Channel) on the y-axis. The PI (Channel) is related to the energy of the photon. There is missing data due to a CCD on RGS1 failing.

bin width in order to over-resolve the spectra. At 2keV the resolution at FWHM is  $\sim 25\text{eV}$  for RGS1 and  $\sim 20\text{eV}$  for RGS2. The filtering and the rebinning of the observations were conducted by running `rgsproc` a second time starting at the filter stage and specifying the GTI table and rebinning parameters. The tool `rgsproc` had to be run on RGS1 and RGS2 separately due to different GTI tables and binning parameters for each of the observations.

### 4.3 Analysis

After filtering and rebinning the data using `rgsproc`, additional grouping of the observations was performed to fit the spectra to a continuum in XSPEC. The

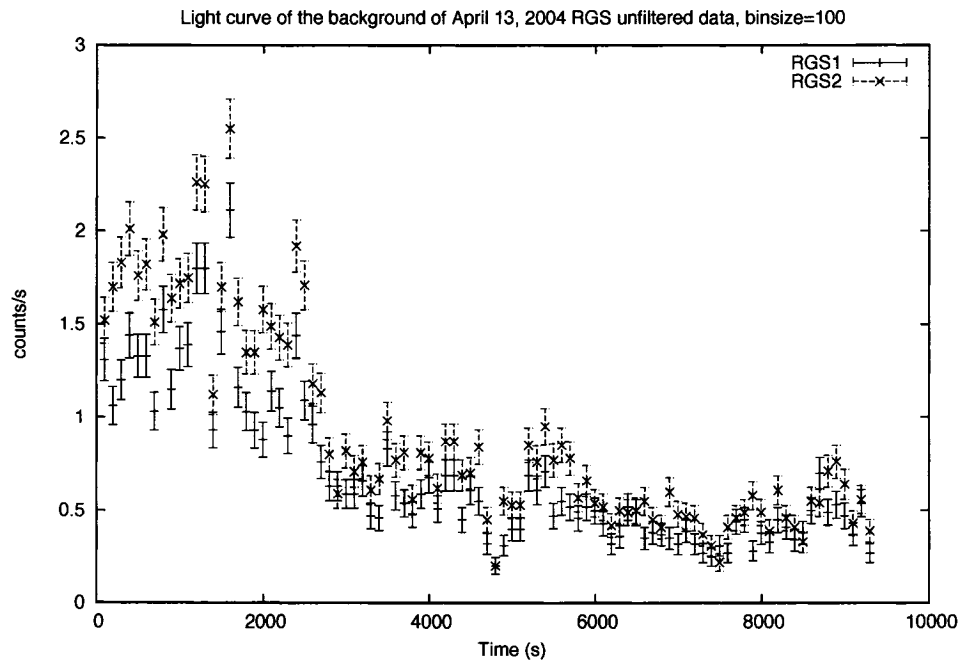


Figure 4-2: The lightcurves of RGS1 and RGS2 on CCD9. The observations are from XMM-1. Time where the count rate was below 1 count/s were stored in a GTI table, which was used to filter the observations.

Table 4–1: Energies Ignored in RGS spectral fits

	Energies(keV)	Comments
XMM-1: April 13, 2004		
RGS1	1.6-1.61	edge of chip 8 (1.18-1.6keV) and 9 (1.61-2.41keV)
RGS2	0.52-0.62	chip 4 missing
	1.23-1.24	edge of chip 7 (0.95-1.23keV) and 8 (1.24-1.71keV)
XMM-2: April 19, 2004		
RGS1	0.72-0.73	edge of chip 5 (0.6-0.72keV) and 6 (0.73-0.90keV)
	1.6-1.61	edge of chip 8 (1.18-1.6keV) and 9 (1.61-2.41keV)
RGS2	0.52-0.62	chip 4 missing
	0.75-0.76	edge of chip 5(0.62-0.75keV) and 6 (0.76-0.94keV)
	0.94-0.95	edge of chip 6 (0.76-0.94keV) and 7 (0.95-1.23keV)
	1.71-1.73	edge of chip 8 (1.24-1.71keV) and (1.73-2.64keV)

The energies which were ignored in the spectral analysis due to data points lying between chips or entire CCD chip missing.

FTOOL `grppha` was used to ensure each bin contained a minimum of 25 counts. A final grouping of each spectrum where the bins with energies above 0.7keV were binned by a factor of four was performed before fitting each spectrum.

When the spectrum of the April 13 and 19, 2004 observations were plotted in XSPEC, there were low lying points which were the result of a missing CCD chip or a data point falling at an energy corresponding to a chip gap that. These would not be representative of the spectrum and the energies where there were the low lying data points were ignored for the spectral fitting. Table 4–1 lists all the low lying data points which were ignored due to chip gaps and missing CCDs.

The spectrum of the two observations and both the RGS1 and the RGS2 were modeled with an absorbed blackbody and an absorbed disk black body. The spectral fitting included a 4% systematic error added to the fit.

#### 4.4 Results

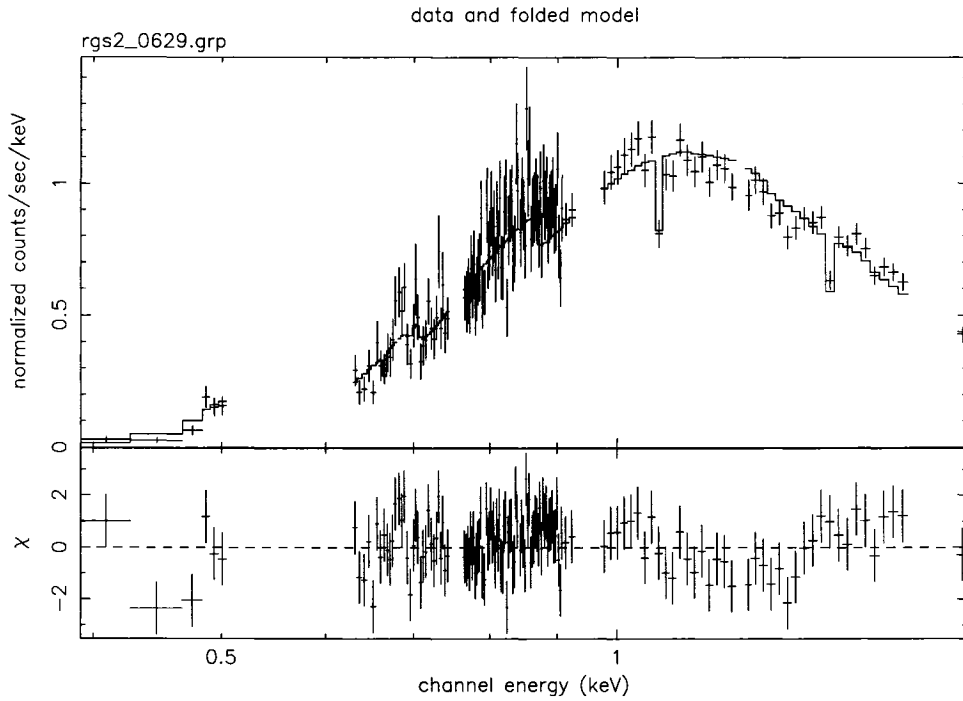
In total there were 8 spectral fits performed. Each observation had two spectra to be modeled: RGS1 and RGS2. There were two observations containing RGS information and two models were used to describe the observations. The RGS1 and RGS2 spectra are not fit jointly, this allows for a line search. Spectral lines are deviations from the continuum, these deviations would be pronounced in the residuals of a spectral fit. If a deviation from the continuum is found in both RGS1 and RGS2, it is strong evidence for a spectral line. For example, in the residual of Figure 4-3 a possible spectral line is indicated at  $\sim 0.82\text{keV}$  for RGS2, but in Figure 4-4 of RGS1 the same feature at  $\sim 0.82\text{keV}$  is not apparent, indicating the feature in RGS2 is not physical.

The spectral fits are summarized in Table 4-2. Both of the models, absorbed blackbody and absorbed disk blackbody, described the observations to equally statistically acceptable levels. The disk blackbody model results in higher flux measurements. Neither spectral model required the addition of a gaussian, which could indicate a spectral line.

#### 4.5 Discussion

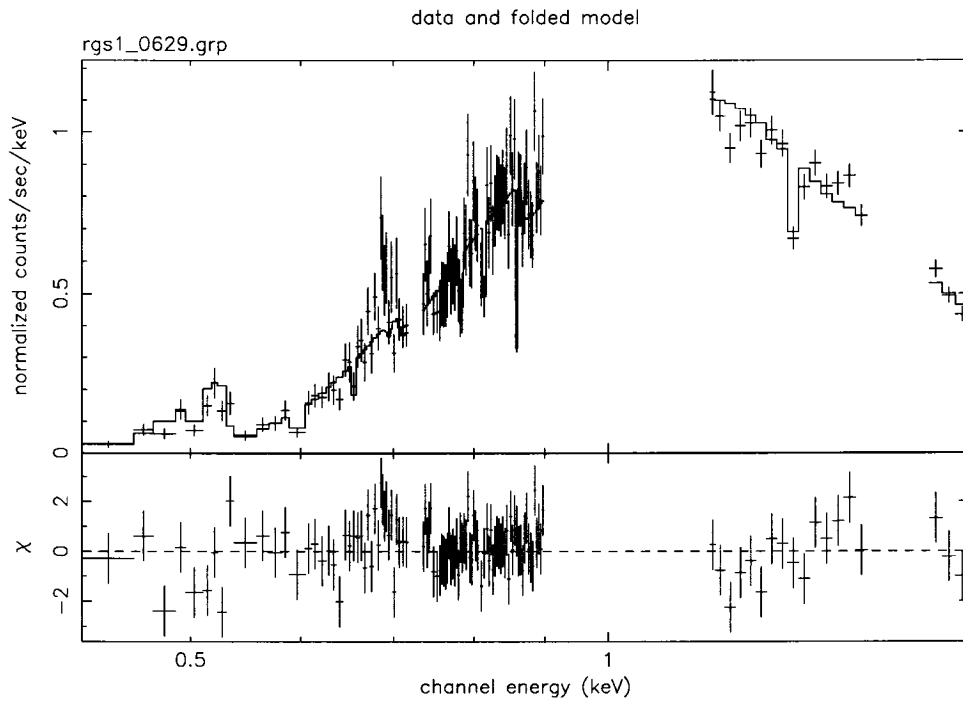
RGS1 and RGS2 from the two observations XMM-1 and XMM-2 are both fit equally well by a continuum model of either an absorbed blackbody or an absorbed disk blackbody. We find no visual evidence of spectral emission lines in either observation.

It should be noted that there are discrepancies between the parameters of the models for the RGS and the EPIC/pn fits in chapter 3. These discrepancies



16-Jun-2006 16:16

Figure 4-3: Spectral fit of an absorbed disk blackbody to the RGS2 data from XMM-2. There appears to be a deviation from the continuum at  $\sim 0.82\text{keV}$ , in the residuals this shows as a low-lying point. This feature is not found in the RGS1 observation (see Figure 4-4) indicating the feature may not be physical.



16-Jun-2006 16:09

Figure 4-4: Spectral fit of an absorbed disk blackbody to the RGS1 data from XMM-2. Comparing to the spectral fit of RGS2 (see Figure 4-3) there is no deviation at  $\sim 0.82$  keV.

Table 4-2: Spectral fits for the two XMM-Newton observations

Parameter	RGS1	RGS2
<b>XMM-1: April 13, 2004</b>		
Absorbed Blackbody		
$N_{H,22}$ (cm <sup>-2</sup> )	0.28±0.03	0.24±0.03
kT (keV)	0.58 <sup>+0.07</sup> <sub>-0.06</sub>	0.64 <sup>+0.07</sup> <sub>-0.08</sub>
$N_{BB}^a$	3.6 <sup>+0.5</sup> <sub>-0.4</sub> × 10 <sup>-3</sup>	3.7 <sup>+0.6</sup> <sub>-0.5</sub> × 10 <sup>-3</sup>
Flux <sup>b</sup>	1.46	1.32
$\chi^2_\nu/\text{dof}(\text{prob})$	0.87/93(0.81)	1.08/130(0.256)
Absorbed Disk blackbody		
$N_{H,22}$ (cm <sup>-2</sup> )	0.39 <sup>+0.04</sup> <sub>-0.02</sub>	0.37±0.01 <sup>d</sup>
$T_{in}$ (keV)	2.0 <sup>+2.9</sup> <sub>-0.9</sub>	3 <sup>+3d</sup> <sub>-1</sub>
$N_{DBB}^c$	2.1 <sup>+10.5</sup> <sub>-2.1</sub>	0.9 <sup>+2.5d</sup> <sub>-0.9</sub>
Flux <sup>b</sup>	1.88	1.75
$\chi^2_\nu/\text{dof}(\text{prob})$	0.85/93(0.84)	1.06/130(0.290)
<b>XMM-2: April 19, 2004</b>		
Absorbed Blackbody		
$N_{H,22}$ (cm <sup>-2</sup> )	0.36 <sup>+0.01</sup> <sub>-0.03</sub>	0.31 <sup>+0.03</sup> <sub>-0.01</sub>
kT (keV)	0.49 <sup>+0.05</sup> <sub>-0.03</sub>	0.55 <sup>+0.03</sup> <sub>-0.06</sub>
$N_{BB}^a$	2.1±0.1 × 10 <sup>-3</sup>	2.2 <sup>+0.1</sup> <sub>-0.2</sub> × 10 <sup>-3</sup>
Flux <sup>b</sup>	1.08	0.94
$\chi^2_\nu/\text{dof}(\text{prob})$	1.06/115(0.30)	1.13/140(0.15)
Absorbed Disk blackbody		
$N_{H,22}$ (cm <sup>-2</sup> )	0.47 <sup>+0.03</sup> <sub>-0.01</sub>	0.44±0.02
$T_{in}$ (keV)	0.98 <sup>+0.36</sup> <sub>-0.11</sub>	1.2 <sup>+0.5</sup> <sub>-0.2</sub>
$N_{DBB}^c$	15.1 <sup>+8.5</sup> <sub>-9.8</sub>	6.9 <sup>+6.7</sup> <sub>-4.6</sub>
Flux <sup>b</sup>	1.41	1.27
$\chi^2_\nu/\text{dof}(\text{prob})$	1.08/115(0.25)	1.07/140(0.28)

Spectral fits of the two RGS units, RGS1 and RGS2, for the two XMM-Newton observations. Fits are to 90% confidence unless otherwise noted.

<sup>a</sup> $L_{39}/D_{10}^2$

<sup>b</sup>unabsorbed flux, × 10<sup>-10</sup>ergs/cm<sup>2</sup>s (0.4-2.0keV)

<sup>c</sup>(( $R_{in}$ /km)/(D/10kpc))<sup>2</sup>cos  $\theta$

<sup>d</sup>1 $\sigma$  error

could be due to a combination of: a lack of cross-calibration of the instruments on *XMM-Newton*<sup>2</sup> and differences in exposure times (for XMM-1: RGS1=7.2ks, RGS2=6.6ks, and EPIC/pn=3.4ks; for XMM-2: RGS1=24.2ks, RGS2=23.8ks, and EPIC/pn=19ks). Another contributing factor to the discrepancies could also be the energy range of the instruments: RGS is not calibrated past 1.9keV, as a result one would not expect a power-law component to be required.

---

<sup>2</sup> see: [http://xmm.vilspa.esa.es/external/xmm\\_sw\\_cal/calib/documentation/index.shtml](http://xmm.vilspa.esa.es/external/xmm_sw_cal/calib/documentation/index.shtml)

## CHAPTER 5 Radius Measurements

### 5.1 Introduction

One way of determining the radius of a neutron star is to fit the spectrum with a thermal model such as a blackbody or hydrogen atmosphere. In the case of Aql X-1, when the system is in quiescence the spectrum can be fit with a hydrogen atmosphere model. As mentioned in Chapter 1, radius measurements can be used to constrain the dEOS for neutron stars. The following section discusses the hydrogen atmosphere model used on the 11 *Chandra* observations of Aql X-1 from Table 3–1. Using the hydrogen atmosphere model to describe the 11 *Chandra* observations, a radius was determined for each individual observation. Also, with these 11 *Chandra* observations of Aql X-1 it was determined if spectral parameters varied between observations. *Chandra* observation 708 had previously been analyzed to determine the radius (Rutledge et al., 2001a). The four *Chandra* observations 708, 709, 710, and 711 had been investigated for variability in spectral parameters (Rutledge et al., 2002b). In this work a similar analysis is performed but using almost three times as many observations of Aql X-1.

### 5.2 Hydrogen Atmosphere Model

Aql X-1 is a LMXB, and as such it has a low magnetic field. The atmospheres of neutron stars with low magnetic fields is covered in Zavlin et al. (1996). For neutron stars with low magnetic fields,  $B \leq 10^8 - 10^{10}$  G, the magnetic field

has a negligible effect on the opacity and the equation of state of the neutron star atmosphere. Like normal stars, the properties of radiation are determined by the radiative transfer in the atmosphere. These properties are dependent on the chemical composition, magnetic field, flux, and gravity at the surface of the star. But, due to the effects of gravity and the large magnetic fields common to neutron stars, the atmospheres of neutron stars are different than those of normal stars. The strong gravity at the neutron star surface causes compression and stratification of the elements in the neutron star atmosphere. Due to the stratification, heavier elements settle out of the atmosphere, leaving the lightest elements such as Hydrogen as the atmosphere. The model spectra of a hydrogen atmospheres differs from a blackbody model in that for the same effective temperature the hydrogen atmosphere models at high (X-ray) energies the spectra is harder, while at lower (UV/optical) energies the flux is lower than the blackbody model. Compared to the hydrogen atmosphere model a blackbody model will overestimate the effective temperature of the X-ray radiation. This overestimate of the effective temperature results in an underestimate of the neutron star radius, as for the same flux measurement,  $R \propto 1/T_{eff}^2$ . With the overestimate of the effective temperature in the blackbody model the radius ends up being underestimated, less than the canonical radius of 10km.

The quiescent LMXBs (qLMXBs) are typically observed to emit 2 components in the X-ray band: a thermal component from the atmosphere of the neutron star and a non-thermal component that is thought to originate from the magnetosphere of the neutron star (Zavlin & Pavlov, 2002). In this work, even though the hydrogen

atmosphere model gives a statistically acceptable fit to individual spectra, when multiple spectra are fit simultaneously the power-law component is required to account for emission above 2keV.

In version 11.3 of XPSEC the hydrogen atmosphere model as calculated in Zavlin et al. (1996) was added as one of the spectral models. The information on the hydrogen atmosphere model in XSPEC is from the XSPEC User's Guide for version 11.3.X, more information of other XSPEC models can be found in the online manual<sup>1</sup>. The hydrogen atmosphere model in XSPEC is called `nsa`. The model allows the user to chose between 3 different magnetic field strengths, non-magnetized ( $B < 10^8$ - $10^9$ G),  $10^{12}$ G, and  $10^{13}$ G. Due to its expected weak magnetic field, the non-magnetized option is used for Aql X-1. With this selection of magnetic field strength the effective temperature can range from  $10^5$  to  $10^7$  K. There are five parameters in the model:  $\log T_{eff}$ ,  $M_\star$ ,  $R_\star$ , the magnetic field strength and a distance parameter. The parameter  $\log T_{eff}$ , which is the unredshifted effective temperature, is related to that which an observer would measure

$$T_{\text{eff}}^\infty = T_{\text{eff}} g_r \quad (5.1)$$

where  $g_r$  is the gravitational redshift factor defined in Chapter 1. The radius measurement given with the atmosphere model,  $R_\star$ , is different from the radiation radius of the neutron star,  $R_\infty$ . The radiation radius is the projected radius of the neutron star as observed from a great distance (eg. at Earth). The radiation radius and  $R_\star$

---

<sup>1</sup> <http://heasarc.gsfc.nasa.gov/docs/xanadu/xspec/xspec11/manual/manual.html>

are related to one another through the gravitational redshift,  $g_r$ :

$$R_\infty = R_\star/g_r \quad (5.2)$$

In the `nsa` model  $M_\star$  is given in units of solar mass and  $R_\star$  is given in units of km. The distance parameter relates to distance as  $1/D^2$ , where  $D$  is the distance to the neutron star measured in pc.

### 5.3 Observations and Data Reduction

There were 11 observations taken of Aql X-1 between the years of 2000 and 2002 with *Chandra* ACIS-S as shown in Table 3–1. In all of these 11 observations Aql X-1 was found to be in quiescence. As described in Chapter 2, the observations were initially reduced by the *Chandra* pipeline, making L1 and L2 event files from the raw data files. The pipeline and calibration version were earlier than the versions available at the time of this work. The L1 event file was reprocessed using CIAO v3.3 and CALDB v3.2.1. The reprocessing of the L1 event file to create a new L2 event file is described in Chapter 2. The only additional change between the reprocessing steps performed and those described in Chapter 2, was if the observation was taken in very faint mode then background cleaning of the L1 event file was included in the data preparation steps. The L2 event files created with CIAO v3.3 and CALDB v3.2.1 were used in the analysis.

### 5.4 Analysis

Light curves and spectra were extracted from each of the 11 *Chandra* observations. The source was extracted from a circular region of radius 5" centered on the coordinates of Aql X-1. The background for both the light curve and the spectra

was extracted from an annulus with an inner radius of  $8''$  and an outer radius of  $25''$  centered on Aql X-1. The lightcurves were binned at 1000s. Examination of the lightcurves show no evidence of variability. Spectral analysis used all the L2 data from each observation. The background spectrum was subtracted from the source spectrum. Each spectra was binned in an identical manner ensuring that the bins were wider than the ACIS energy resolution. The data below 0.5keV and above 8keV were excluded from analysis. Also, the data points between 0.5-2.11keV were binned so that each bin was 0.15keV wide, from 2.11-4keV the bins were 1.9keV wide and from 4-8keV the bins were 2keV wide, resulting in 13 bins. Using this binned data the individual spectra were fit to an absorbed hydrogen atmosphere model in XSPEC v11.3.1. The absorption model fits for the equivalent of the hydrogen column between the observer and the source. A 4% systematic uncertainty was assumed in the fitting of each of the observations. Fitting each observation individually with the absorbed hydrogen atmosphere model resulted in a radius measurement and effective temperature of Aql X-1 in each observation.

To investigate the possibility that spectral parameters changed from observation to observation, all the observations were fit simultaneously. When the spectra of the 11 *Chandra* observations were fit simultaneously a power-law was required in addition to the absorbed hydrogen atmosphere. The power-law model fits for the power-law index and a normalization factor which is measured in photons/keV/cm<sup>2</sup>/s at 1keV. Initially when simultaneously fitting the 11 *Chandra* observations just an absorbed hydrogen atmosphere model was used and only a single parameter was allowed to vary at a time between observations. As the hydrogen atmosphere model

did not give statistically acceptable fits, a power-law component was added. With the absorbed hydrogen atmosphere with a power-law model initially only one parameter was allowed to vary between observations. As statistically acceptable fits were not made with this method, both the power law components were then allowed to vary between observations.

## 5.5 Results

### 5.5.1 Individual Observation Spectral fits

Fitting each individual spectrum with an absorbed hydrogen atmosphere model resulted in statistically acceptable fits in 8 of 11 observations. Figure 5-1 displays the fit of the 11 *Chandra* observations, including the three which were not statistically acceptable. From the residuals it is apparent that the high-energy channels are biasing the fits. Since the absorbed hydrogen model described the spectra, a power-law component was not added to the model. The addition of the power-law is addressed in the next section where the 11 observations are jointly fit. The best fit parameters for each of the observations are listed in Table 5-1. The parameters are also summarized graphically in Figure 5-2. The flux measurements were consistent with Aql X-1 being in quiescence. For each observation a radius measurement was obtained, where  $R_*$  is the physical radius and  $R_\infty$  is the radiation radius. The physical radius,  $R_*$ , the radiation radius,  $R_\infty$ , are both listed in Table 5-1. But, as displayed in Figure 1-1, for a specific  $R_\infty$  value there are two values of  $R_*$  for a single  $M_*$  value: a lower and upper  $R_*$  measurement. In this spectral analysis the lower  $R_*$  values are disallowed by causality. The Table lists the upper  $R_*$  values, which are permitted. In the *nsa*, hydrogen atmosphere model the radius measurement

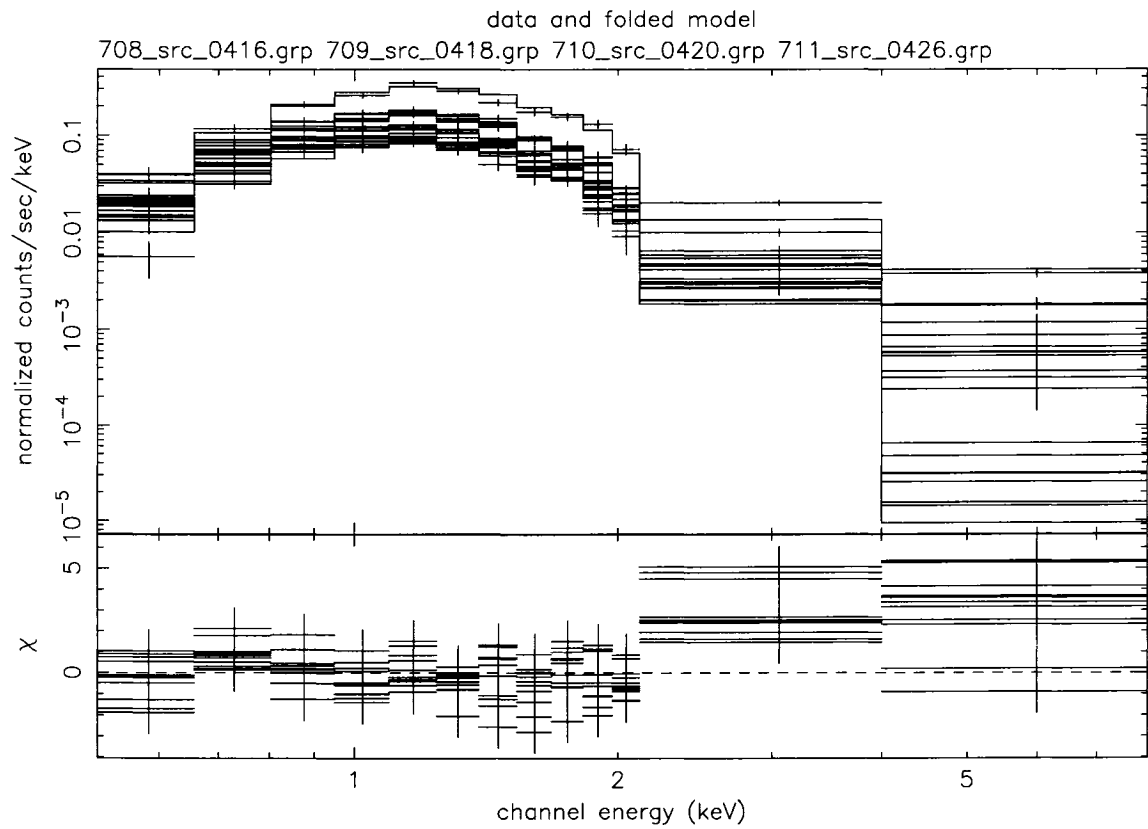
can fall between the model defined hard limits of 5-20km. The radius values of the statistically acceptable fits agree with each other within error.

### 5.5.2 Multiple Observation Spectral fits

While spectra from most of the 11 individual observations can be fit to a statistically acceptable level with only an absorbed hydrogen atmosphere model, this is not the case when all 11 observations are fit jointly.

Using an absorbed hydrogen atmosphere model holding all parameters the same for each of the 11 observations is statistically unacceptable. This is obvious from the fact that count rate are significantly different observation to observation, and therefore the fluxes are significantly different. In addition, a joint fit permitting only  $N_{H,22}$  to vary fails statistically ( $\chi^2_{\nu} / \text{dof} = 8.54/130$ , prob.=0.0); as does permitting only  $\text{Log}T_{eff}$  to vary ( $\chi^2_{\nu} / \text{dof} = 2.06/130$ , prob.= $1.43 \times 10^{-11}$ ), or  $R_{\star}$  ( $\chi^2_{\nu} / \text{dof} = 2.70/130$ , prob.= $3.29 \times 10^{-22}$ ). Examination of Figure 5-3 , as well as the residuals of the spectral fits reveals why none of these single-parameter variations acceptably explain the data: there is significant emission at energies  $>2\text{keV}$ , which varies between observations. There is no acceptable thermal model which can explain this high energy emission, which therefore requires an additional component to explain it, as has been done in much previous work. A power-law is used to parameterize the additional component.

Adding a power-law component to the model and jointly fitting all the observations is insufficient to explain the data. A model of absorption plus a hydrogen atmosphere, plus a power-law component is used to explain the high energy emission, for a total of five free parameters. A model in which all five parameters are jointly fit



hoffmank 27-Sep-2006 23:12

Figure 5-1: The spectral fits and residuals to the 11 *Chandra* observations being fit by an absorbed hydrogen atmosphere. This includes the eight observations that had statistically acceptable fits and the three that were not fit to a statistically acceptable level. The residuals indicate that the high-energy channels are biasing the fits.

Table 5-1: Best fit H-atmosphere model parameters to individual *Chandra* observations of Aql X-1

Obs ID	$N_{H,22}$ ( $\text{cm}^{-2}$ )	$\text{Log}T_{eff}$ K	$R_*$ (D/5kpc)km	$R_\infty$ (D/5kpc)km	Flux ( $10^{-13} \text{ erg s}^{-1}$ )	$\chi^2_\nu / \text{dof}(\text{prob})$
708	$0.45 \pm 0.04$	$6.51^{+0.03}_{-0.05}$	$7.1^{+0.4}_{-0.2}$	$11.0^{+0.8}_{-0.5}$	8.25	1.37/10(0.187)
709	$0.49^{+0.05}_{-0.04}$	$6.50^{+0.03}_{-0.04}$	$8.0^{+0.3}_{-0.2}$	$11.5^{+0.7}_{-0.5}$	4.73	1.12/10(0.344)
710	$0.49 \pm 0.04$	$6.53 \pm 0.02$	$8.0^{+0.3}_{-0.2}$	$11.5^{+0.7}_{-0.5}$	6.82	1.18/10(0.30)
711	$0.51^{+0.04}_{-0.03}$	$6.55 \pm 0.01$	$8.61^{+0.07a}_{-0.02}$	$11.94^{+0.17a}_{-0.05}$	7.47	3.34/10( $2.30 \times 10^{-4}$ )
3484	$0.49^{+0.04}_{-0.03}$	$6.57^{+0.02}_{-0.03}$	$8.3^{+0.2a}_{-0.1}$	$11.7^{+0.5a}_{-0.2}$	10.19	1.65/10(0.09)
3485	$0.49^{+0.04}_{-0.03}$	$5.594^{+0.014}_{-0.004}$	$8.70^{+0.08a}_{-0.00}$	$12.01^{+0.19a}_{-0.00}$	12.67	3.73/10( $5.03 \times 10^{-5}$ )
3486	$0.49 \pm 0.03$	$6.64 \pm 0.01$	$8.42^{+0.05a}_{-0.07}$	$11.8^{+0.1a}_{-0.2}$	27.14	3.97/10( $1.93 \times 10^{-5}$ )
3487	$0.43 \pm 0.05$	$6.48^{+0.04}_{-0.05}$	$7.7^{+0.5}_{-0.2}$	$11.3^{+1.1}_{-0.4}$	4.58	1.82/10(0.052)
3488	$0.50 \pm 0.05$	$6.53^{+0.01}_{-0.04}$	$8.3^{+0.2a}_{-0.1}$	$11.7^{+0.5a}_{-0.2}$	5.38	1.27/10(0.241)
3489	$0.53 \pm 0.05$	$6.48^{+0.02}_{-0.05}$	$7.5^{+0.5}_{-0.2}$	$11.2^{+1.1}_{-0.4}$	3.90	1.37/10(0.185)
3490	$0.50^{+0.05}_{-0.04}$	$6.52 \pm 0.03$	$8.0^{+0.3}_{-0.2}$	$11.5^{+0.7}_{-0.5}$	5.78	1.99/10(0.03)

The spectra of each *Chandra* observation was fit to a model which described a neutron star with a hydrogen atmosphere. The model fits for a radius and effective temperature of the neutron star. The neutron star radius is given in column  $R_*$ , and the radiation radius is given in column  $R_\infty$ . All the uncertainties are 90% confidence. The X-ray fluxes are the absorbed flux over the range 0.5-10keV. Assumed source distance of 5kpc.

<sup>a</sup> reached hard limit

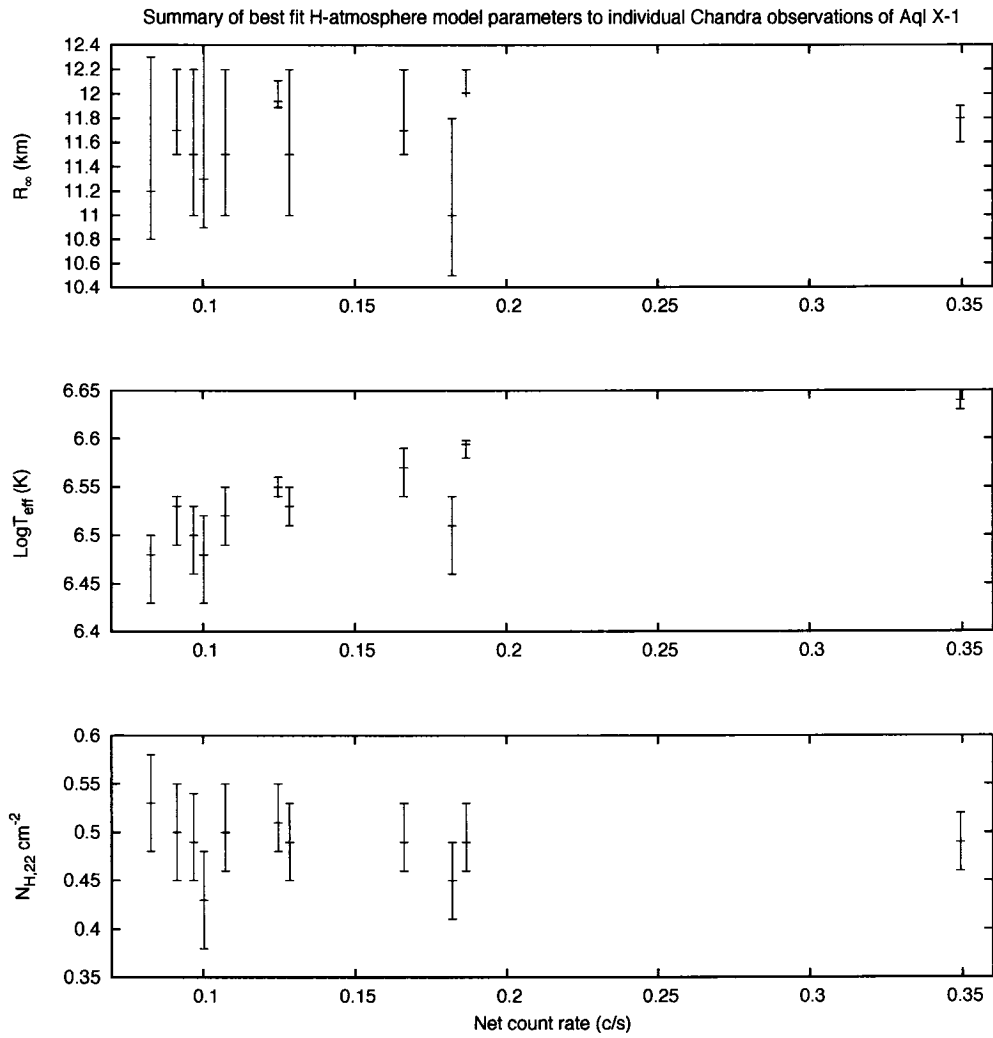


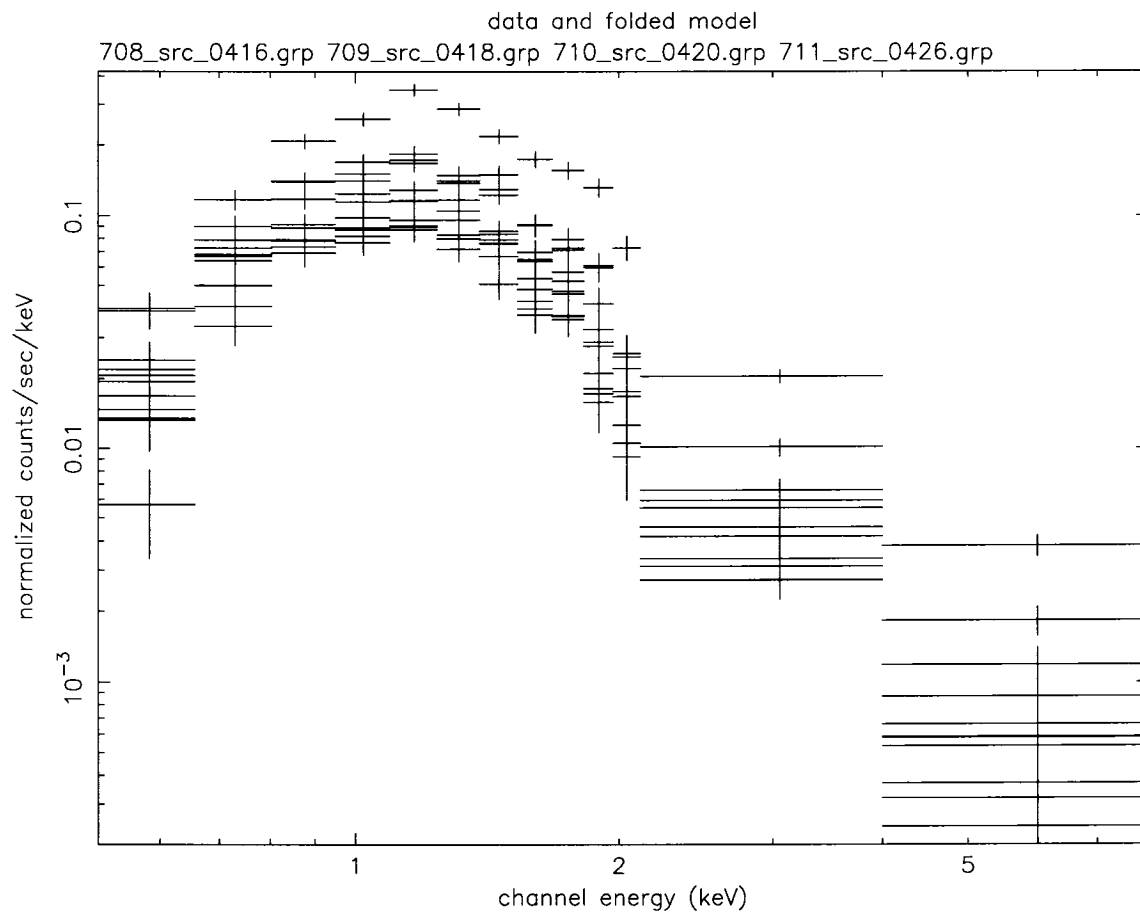
Figure 5-2: A summary from the individual spectral fits of the measured radiation radius,  $R_\infty$ , log of effective temperature and absorption as a function of the net count rate. An absorbed hydrogen atmosphere was used for the spectral fitting. All 11 best fit parameters are displayed even those which did not have statistically acceptable fits.

between observations is statistically unacceptable ( $\chi^2_{\nu} / \text{dof} = 12.26/138$ ,  $\text{prob.} = 0.0$ ). Moreover, permitting one parameter to vary between the 11 observations, while allowing the other four parameters to jointly fit, also does not explain the data; of these five possible fits, the most statistically acceptable fit was one permitting the parameter  $\text{Log}\Gamma_{eff}$  to vary ( $\chi^2_{\nu} / \text{dof} = 1.53/128$ ,  $\text{prob.} = 9.73 \times 10^{-5}$ ).

However, when a model is adopted in which the absorption and hydrogen atmosphere parameters are jointly fit, but the normalization and the slope of the power-law are permitted to vary, a statistically acceptable fit is found. The spectral fits and the residuals from the joint fit are displayed in figure 5-4. The residuals in figure 5-4 do not indicate any significant systematic trend in the joint fit. Therefore this model is adopted to explain the data. Table 5-2 contains the results for this fit. Figure 5-5 shows how the photon index and power-law normalization change with intensity (net count rate). Both the photon index and the power-law normalization as a function of count rate were fit to a straight line. In the case of the photon index as a function of count rate the slope is -2.6: the photon index decreases with increasing intensity. For the power-law normalization the slope of the straight line fit was found to be 0.004: the power-law normalization,  $N_{pl}$ , increases with increasing intensity.

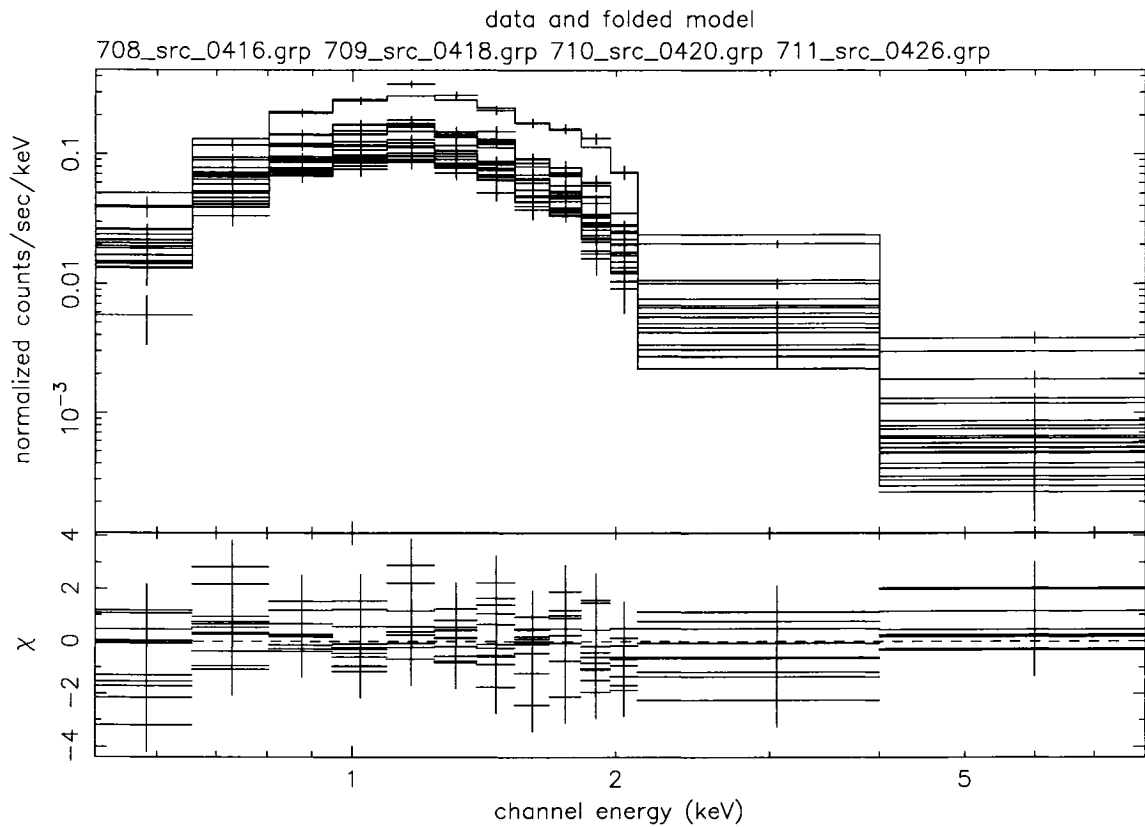
## 5.6 Discussion

The 11 *Chandra* observations all caught Aql X-1 in a state of quiescence. The observations of Aql X-1 individually were well described by an absorbed hydrogen atmosphere model. The radius measurements are all statistically consistent with best fit values.



27-May-2006 19:29

Figure 5-3: The extracted spectra of each of the 11 *Chandra* observations of Aql X-1. The spectra are both fit to a model in this Figure. While it is not possible to see the spectra individually here, the figure makes plain the amount of variability as a function of photon energy observed between observations. The high energy (>2keV) portion varies over and order of one magnitude.



hoffmank 27-Sep-2006 23:20

Figure 5-4: The spectral fits of the 11 *Chandra* observations fit to an absorbed hydrogen atmosphere with a power-law. The two power-law components – slope and normalization – were permitted to vary between observations. The residuals do not indicate a systematic trend in the spectral fits.

Table 5-2: Spectral Parameters for All *Chandra* observations of Aql X-1 with varying power-law spectral component

Obs ID	$N_{H,22}$ ( $\text{cm}^{-2}$ )	$\text{Log}T_{eff}$ (K)	$R_*$ (D/5kpc) (km)	$R_\infty$ (D/5kpc) (km)	$\alpha$	$N_{pl}$ (photons $\text{cm}^{-2}\text{s}^{-1}$ at 1keV)	$\chi^2_\nu/\text{dof}$ (prob)
708	$0.57^{+0.06}_{-0.06}$	$6.49^{+0.01}_{-0.02}$	$8.14^{+0.15}_{-0.06}$	$11.6^{+0.4}_{-0.1}$	$3.59^{+0.30}_{-0.31}$	$6.48^{+2.44}_{-2.11} \times 10^{-4}$	1.23/118(0.04)
709					$3.83^{+0.72}_{-0.98}$	$1.86^{+1.61}_{-1.26} \times 10^{-4}$	
710					$3.46^{+0.40}_{-0.26}$	$3.48^{+1.90}_{-1.44} \times 10^{-4}$	
711					$3.09^{+0.46}_{-0.63}$	$2.87^{+1.81}_{-1.42} \times 10^{-4}$	
3484					$3.35^{+0.33}_{-0.38}$	$5.76^{+1.18}_{-1.86} \times 10^{-4}$	
3485					$3.08^{+0.33}_{-0.38}$	$6.41^{+2.42}_{-1.93} \times 10^{-4}$	
3486					$2.95^{+0.22}_{-0.27}$	$1.42^{+0.22}_{-0.31} \times 10^{-3}$	
3487					$4.27^{+0.73}_{-0.59}$	$2.62^{+0.88}_{-1.36} \times 10^{-4}$	
3488					$3.74^{+0.69}_{-1.46}$	$1.76^{+0.83}_{-1.32} \times 10^{-4}$	
3489					$3.55^{+1.33}_{-1.22}$	$1.08^{+0.42}_{-0.97} \times 10^{-4}$	
3490					$3.43^{+0.47}_{-0.63}$	$2.62^{+0.89}_{-1.38} \times 10^{-4}$	

Fitting all *Chandra* observations of Aql X-1 simultaneously to a hydrogen atmosphere model with a power-law. Both power-law components were allowed to vary between observation while the absorption and the atmosphere parameters were the same for all observations. All the uncertainties are 90%. Assumed the source distance is 5kpc. Mass was held constant at 1.4 solar masses and the magnetic field was set to 0 G in the hydrogen atmosphere.

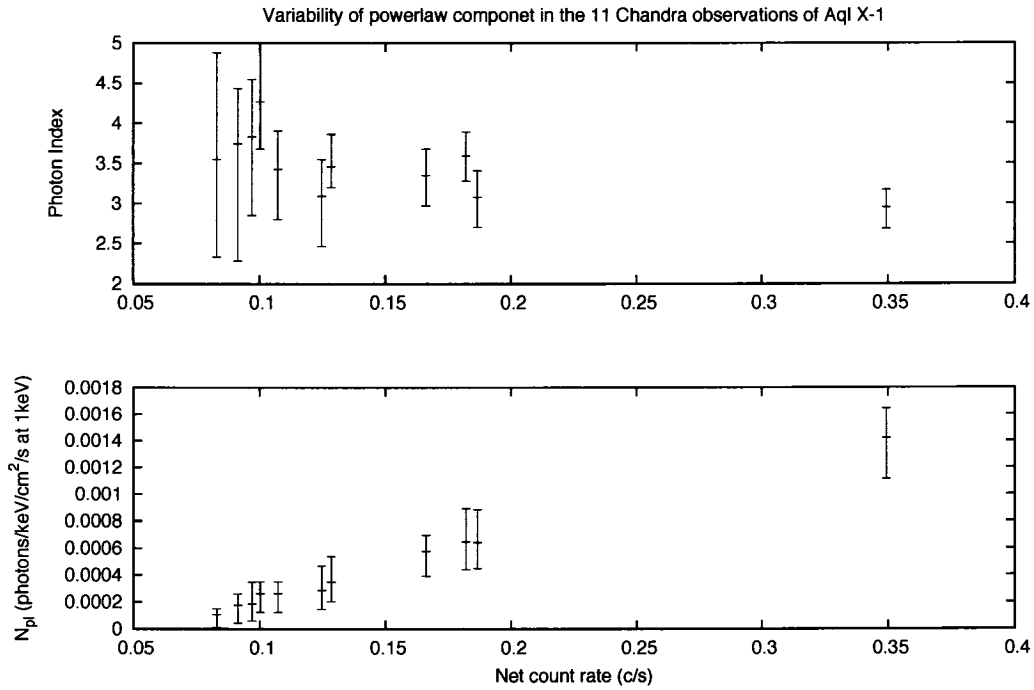


Figure 5-5: The varying power-law components as a function of count rate from the simultaneous spectral fit of the 11 *Chandra* observations. An absorbed hydrogen atmosphere with a power-law was used for the simultaneous fit. Both of the power-law parameters were allowed to vary between observations. Each of the plot were parametrized with a straight line:  $y=mx+b$ , in the case of the photon index the slope is  $-2.56$ , and the slope for  $N_{pl}$  is  $0.004$ . In the top figure the photon index decreases with increasing countrate. In the lower figure the powerlaw normalization,  $N_{pl}$ , increases with increasing countrate.

Fitting all the 11 observations jointly required the addition of the a powerlaw component to account for emission at photon energies  $>2\text{keV}$ . It was found that allowing both powerlaw parameters ( $\alpha, N_{PL}$ ) to vary between observations provided a statistically acceptable fit. With increasing count rate the powerlaw index decreased and the powerlaw normalization increased. The 11 Chandra observations of Aql X-1 were found to have a constant thermal component with a variable high energy component. The high energy component was parameterized as a powerlaw. The best fit radius measurement of Aql X-1 is  $R_\infty=11.6_{-0.1}^{+0.4}\text{km}$  from the 11 jointly fit observations where the thermal component was constant and the high photon energies ( $>2\text{keV}$ ) were parameterized by a varying powerlaw.

Previously, a varying powerlaw along with a varying column density had been noted in Aql X-1 (Campana & Stella, 2003). For this claim the *Chandra* observations 708, 709, 710, and 711 as well as a *BeppoSaX* observation were utilized. This result is not in agreement with the present analysis, where just a varying powerlaw is found in Aql X-1. In this present work  $\sim$ twice as many observations of Aql X-1 were used, spanning  $\sim$ two years (versus five months). The reason for a varying powerlaw is unclear since the physics process that results in the existence of a powerlaw in a spectrum is poorly understood.

## CHAPTER 6 RRATs

### 6.1 Introduction

A new population of neutron stars has been recently introduced (McLaughlin et al., 2005). This population – called Rotating RAdio Transients (RRATs) – were detected in observations which were part of the Parkes Multibeam Pulsar survey, and were discovered by searching for isolated radio bursts. Eleven sources were identified. These 11 RRATs are characterized by bursts of radio emission (at 1.4 GHz) that last between 2 and 30 ms. The time between radio bursts ranges from 4 minutes to 3 hours. Of the 11 RRATs, all were observed to burst at least 4 times with the most prolific burster being detected 229 times. The positional uncertainties span a wide range: from 0.6 arcsec to 7 arcmin.

One of the 11 RRATs identified, J1819-1458 was subsequently reported to have a X-ray counterpart (CXOU J181934.1-145804) (Reynolds et al., 2005). This counterpart was serendipitously observed in a *Chandra* observation. The counterpart was described by a thermal spectrum, with emission consistent with a cooling neutron star with a characteristic age of  $10^4$ - $10^5$  years. The radio source, J1819-1458, had a measured  $\dot{P}$  which implies a characteristic age of 117kyr, consistent with that of the X-ray counterpart assuming it is a cooling neutron star. Thus, the characteristic ages of the X-ray counterpart and J1819-1458 were consistent with each other. With the

consistent characteristic age measurements of CXOU J181934.1-145804 and its position to the RRAT position, it was designated the X-ray counterpart to the RRAT, J1819-1458 (Reynolds et al., 2005).

Of the 11 RRATs, one – J1911+00 – is  $\sim 2$  arcmin from the position of Aql X-1 with an error box of 15 arcmin (in right ascension) by 7 arcmin (in declination). Thus, the *Chandra* or *XMM-Newton* observations of Aql X-1 may contain the X-ray counterpart of a RRAT. In addition, we may investigate the possibility that Aql X-1 is a RRAT.

The emission mechanism of the RRATs is highly uncertain, and so it is difficult to predict what the X-ray properties of the counterpart should be. However, given the transient, short time-scale radio bursts, possible properties to look for to discover candidate X-ray counterparts include:

1. an unusually bright X-ray source in the error circle, to distinguish it from the random presence of field sources,
2. evidence of transient X-ray emission,
3. and evidence of non-thermal X-ray emission.

Since RRATs are radio sources the non-thermal X-ray emission is expected: radio emission is thought to arise from the magnetosphere of the neutron star. If the X-ray emission also arose from the magnetosphere the result would be non-thermal emission (Manchester, 2004). Though non-thermal emission is expected due to radio emission, thermal emission could also arise if the neutron star was in a different state.

It should be noted that all three of the three criteria apply to Aql X-1, and so new behavior from Aql X-1 which might tie it to the RRAT was searched for.

X-ray sources in the field which exhibited the above properties were also searched for. No new behavior in Aql X-1 which would tie it to RRAT 1911+00 was found. However, a transient X-ray source in the FOV was discovered which has no optical/IR counterpart in the 2MASS All Sky Survey, which suggests it as the candidate X-ray counterpart.

## 6.2 Observations and Analysis

These are the same observations that were used in previous chapters (see Table 3-1). All 13 observations were examined possible counterparts to the RRAT in the field of view of the Aql X-1 observation. *XMM-Newton* RGS was not used in the analysis in this chapter.

Since bursting activity would result in pileup, events associated with a candidate counterpart to a RRAT may have been flagged as a cosmic ray event and filtered out of the observational data. To search for sources in the *Chandra* observations the CIAO tool `celldetect` was used on the L1 event observations. The tool `celldetect`<sup>1</sup> searches for sources using a sliding cell. The counts in the cell are summed and compared to the background. If the the signal-to-noise ratio comparing source and background counts is above the specified detection threshold a source is recorded. The background is estimated from a cell surrounding the sliding detection cell. A signal-to-noise ratio of 4 was used as the detection for the source search in the *Chandra* observation.

---

<sup>1</sup> for more information see website: <http://cxc.harvard.edu/ciao/ahelp/celldetect.html>

Once a list of sources in the *Chandra* observations was compiled, optical counterparts were searched for in the 2MASS All-sky survey and USNO-B1.0 catalogues.

Bursting activity from sources in the FOV of the Aql X-1 *Chandra* observations were investigated by comparing the high PI channels in all sources, including Aql X-1, to the background. Due to the time resolution of the observations a burst event would result in excess counts in the high PI channels. These events would be flagged as cosmic ray events and filtered out in the L2 event files. The L1 event files from the *Chandra* observations were checked for counts in the PI channels.

Candidate counterparts were characterized by extracting and fitting a spectrum from the L2 event files. The extracted spectrum was fit to an absorbed blackbody and an absorbed power-law. A systematic uncertainty of 4% was applied to the fit and the absorption was held constant.

The sources detected in the *Chandra* observations were compared to the same coordinates in the *XMM-Newton* observations. With the comparison a calculation of the flux upper limit for the two *XMM-Newton* observations can be made.

## 6.3 Results

### 6.3.1 *Chandra* Source Search

After running `celldetect` on all 11 *Chandra* observations, only one observation had more than one source detected. In the 10 observations where only one source was detected, the source was Aql X-1. *Chandra* observation 709 had two sources detected (Table 6–1). Source 2 was identified as Aql X-1. The catalogues: 2MASS

Table 6–1: Sources detected in Chandra Observation 709

Source	RA	DEC
1	$19^h11^m21.367^s \pm 0.004s$	$00^\circ38'43''.69 \pm 0.05''$
2	$19^h11^m16.006^s \pm 0.002s$	$00^\circ35'05''.16 \pm 0.04''$

Source 2 was identified as Aql X-1. The uncertainties listed are only the statistical uncertainty. The systematic uncertainty is  $0.6'' = 1\sigma$ . The catalogues: 2MASS All-sky survey and UNSO-B1.0 were checked in order to identify source 1. An object was not found listed in the two catalogues at the coordinates of source 1. Source 1 is designated the name CXOU J191121.4+003844.

All-sky survey (Skrutskie et al., 2006) and USNO-B1.0<sup>2</sup> were checked for an identified object at the coordinates of source 1. For both catalogues a circle with a 2 arcsec radius centered on the location of source 1 was searched for possible optical/UV counterparts. For both of the catalogues the search was negative, a counterpart was not listed in the catalogues at the source 1 coordinates. The source 1 detected in the *Chandra* observation 709 is designated by the name CXOU J191121.4+003844.

### 6.3.2 CXOU J191121.4+003844

Since CXOU J191121.4+003844 falls within the error circle of the RRAT J1911+00 and CXOU J191121.4+003844 is also not listed in either the 2MASS All-sky survey or the UNSO-B1.0 catalogues, it warrants further investigation. The high PI channels from the L1 event file of CXOU J191121.4+003844 were all checked for excess counts, see Figure 6–1. In Figure 6–1 the PI channels for CXOU J191121.4+003844 were compared to those of Aql X-1 and the background from the same observation, 709. The counts were extracted from a 4 arcsec radius circular region of CXOU

---

<sup>2</sup> see <http://www.nofs.navy.mil/data/fchipx>

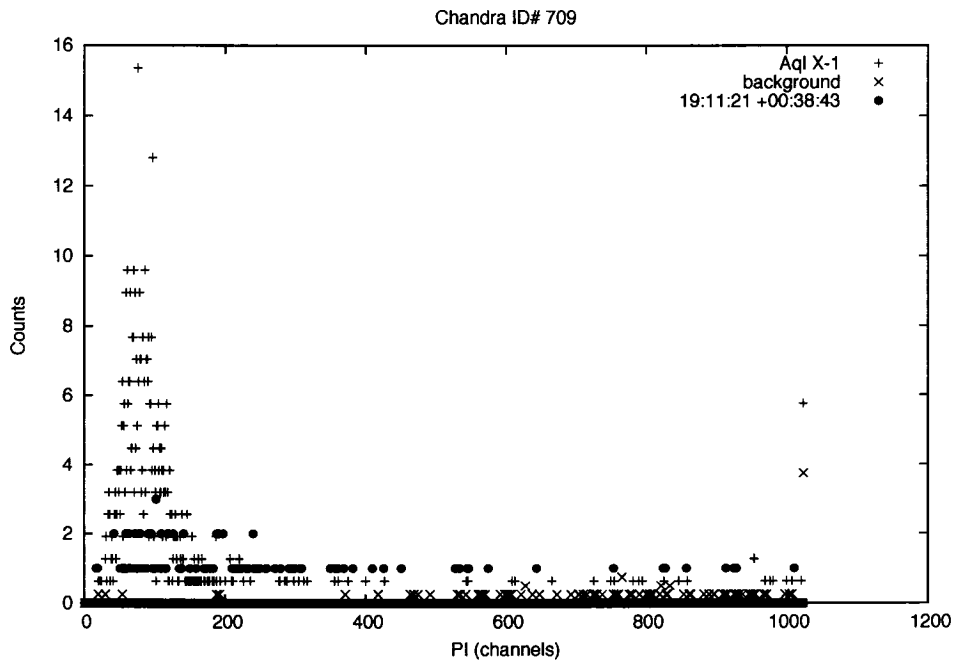


Figure 6-1: Comparing the L1 high PI counts for CXOU J191121.4+003844, Aql X-1, and the background. All counts were area corrected to the area of extraction of CXOU J191121.4+003844. CXOU J191121.4+003844 does not display an excess of counts over the background in the high PI channels.

J191121.4+003844 and a 5 arcsec radius circular region for Aql X-1. Both circular regions were centered on the coordinates of the respective source. The background was extracted from a 8 arcsec circular region away from both CXOU J191121.4+003844 and Aql X-1. CXOU J191121.4+003844 does not display an excess of counts in the high PI channel over the background.

A spectrum of CXOU J191121.4+003844 was extracted from the L2 event file of the Chandra observation 709. The spectrum consisted of only 100 counts from the source and the background. Since the number of background counts expected in the source regions is  $\sim 3$ , the background is low enough that it does not need to

be subtracted from the source for spectral fitting. The spectrum was extracted from a 4 arcsec radius circle centered on CXOU J191121.4+003844. The spectrum was grouped to ensure there was between 18 and 21 counts in each bin.

The results of the spectral fitting are given in Table 6–2. The spectrum was fit to an absorbed blackbody and an absorbed power-law. The absorption for all three spectral fits was fixed at a value of  $0.33 \times 10^{22} \text{cm}^{-2}$ . The value for the absorption was calculated using the HEASARC tool `nH3` which calculates the total galactic HI column density as a function of direction. The column density was calculated for Aql X-1 and this value was then used for CXOU J191121.4+003844.

Fitting the spectrum of CXOU J191121.4+003844 with an absorbed power-law gave the best fit of the three models. The photon index of the power-law describing the spectrum of CXOU J191121.4+003844 was found to be  $1.0_{-0.4}^{+0.3}$ . Figure 6–2 displays the spectral fit of the absorbed power-law model to the extracted spectrum of CXOU J191121.4+003844. This unabsorbed flux for the absorbed power-law corresponds to a luminosity of  $2.4 \times 10^{32} \text{ergs}^{-1}$  (d/3.3kpc), at the 3.3 kpc distance determined by  $N_e$  (McLaughlin et al., 2005).

With the flux from the spectral fit of CXOU J191121.4+003844 and a limiting magnitude of USNO-B1.0, an X-ray to optical flux can be estimated. Since CXOU J191121.4+003844 was not listed in the USNO-B1.0 catalogue, it must be fainter than the detection threshold contained in the catalogue. The USNO-B1.0 catalogue contains a listing of objects using all-sky coverage down to a magnitude of  $V=21$

---

<sup>3</sup> see <http://heasarc.gsfc.nasa.gov>

Table 6–2: Spectral fits to CXOU J191121.4+003844

Model: Absorbed Blackbody	
$N_{H,22}(\text{cm}^{-2})$	(0.33)
kT (keV)	$1.2_{-0.4}^{+0.3}$
$N_{BB}^a$	$1.91_{-0.69}^{+1.05} \times 10^{-6}$
Model flux <sup>b</sup>	$1.43 \times 10^{-13}$
$\chi^2_{\nu}/\text{dof}(\text{prob})$	4.47/3( $3.83 \times 10^{-3}$ )
Model: Absorbed Powerlaw	
$N_{H,22}(\text{cm}^{-2})$	(0.33)
$\alpha^c$	$1.0_{-0.4}^{+0.3}$
$N_{PL}^d$	$1.5_{-0.4}^{+0.5} \times 10^{-5}$
Model Flux <sup>b</sup>	$1.79 \times 10^{-13}$
$\chi^2_{\nu}/\text{dof}(\text{prob})$	0.646/3(0.585)

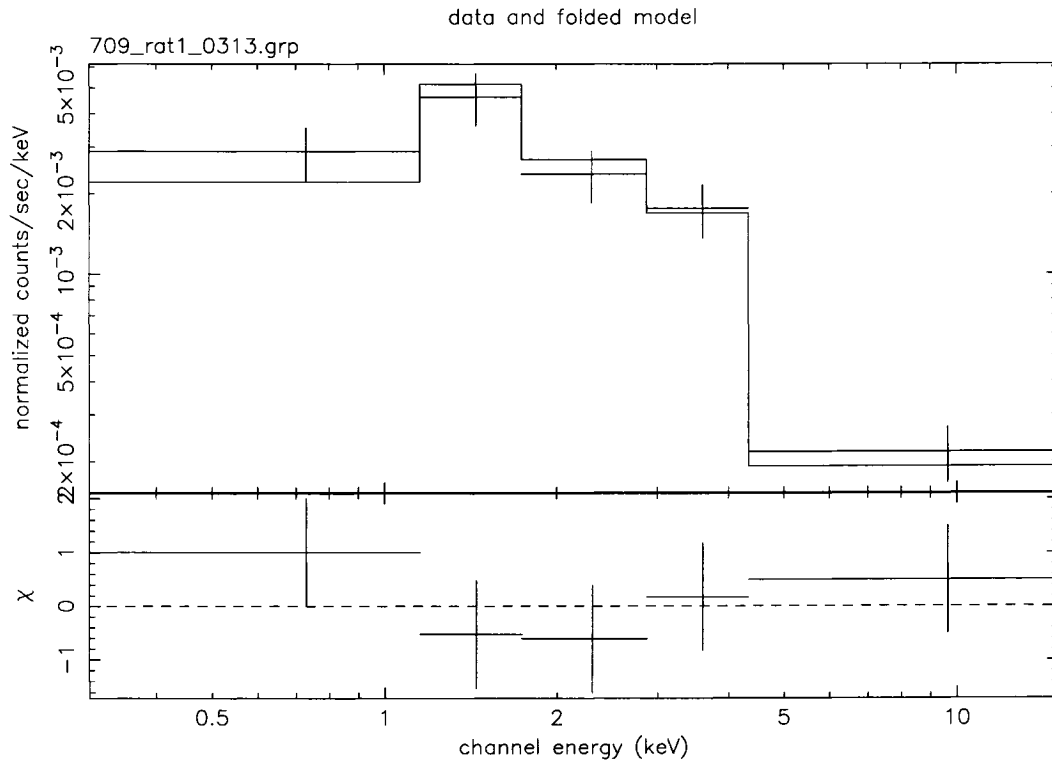
The spectral parameter fits to the CXOU J191121.4+003844 spectrum extracted from the L2 event file of *Chandra* observation 709. The extracted spectrum contained 100 counts and the background was not subtracted. All errors are 90% confidence.

<sup>a</sup>  $L_{39}/D_{10}^2$

<sup>b</sup> unabsorbed flux,  $\text{ergs cm}^{-2}\text{s}^{-1}$  (0.5-8.0keV)

<sup>c</sup> power-law index

<sup>d</sup> photons  $\text{cm}^{-2}\text{s}^{-1}$  at 1keV



3-Jun-2006 15:13

Figure 6-2: The best fit spectral model to CXOU J191121.4+003844 was an absorbed power-law. That absorption was held fixed while the two power-law components were allowed to vary. The spectrum was extracted from the L2 event file of *Chandra* observation 709. The spectrum of CXOU J191121.4+003844 contained 100 counts, these were binned such that each bin contained between 18 and 21 counts.

(Monet et al., 2003). The corresponding flux to a magnitude of V=21 sets an upper limit to the optical flux of CXOU J191121.4+003844. The ratio between the unabsorbed flux of CXOU J191121.4+003844 from the absorbed power-law fit and the upper limit flux is:  $f_x/f_{opt} \geq 13.5$ . This ratio indicates CXOU J191121.4+003844 could possibly be an AGN, a cluster, or a CV/X-ray binary, but not a white dwarf or a star<sup>4</sup>. The number of AGN predicted is  $\sim 0.3$  at the X-ray flux of CXOU J191121.4+003844 over 2-10keV ( $1.9 \times 10^{-13}$  erg cm<sup>-2</sup> s<sup>-1</sup>) within a FOV of 15'×7' (Hasinger et al., 2001), indicating that CXOU J191121.4+003844 cannot be excluded as a background AGN.

The *XMM-Newton* EPIC/pn observations XMM-1 and XMM-2 were used to further characterize CXOU J191121.4+003844. From both unfiltered *XMM-Newton* observations counts were extracted from a circular region of 15 arcsec radius centered on CXOU J191121.4+003844. Background counts were extracted from an annulus of a 20 arcsec inner radius and a 40 arcsec outer radius. The signal-to-noise ratio (S/N) for XMM-1 is 1.5 and for XMM-2 the S/N is 1.9. Table 6–3 summarizes the extracted counts. In neither *XMM-Newton* observation is there a detection of CXOU J191121.4+003844.

The S/N ratio was calculated using the formula (Pivovarov, 2000):

$$S/N = \frac{S}{\sqrt{S + b(1 + \beta)}} \quad (6.1)$$

where:

---

<sup>4</sup> <http://heasarc.gsfc.nasa.gov/wgacat>

Table 6–3: CXOU J191121.4+003844 source and background counts in both *XMM-Newton* observations

Region	XMM-1	XMM-2
source	27±18	34±18
background	256±7	240±7

Source counts are the counts above the background. The background counts have been area corrected to the source region area.

$S$  :  $N_s - b$ , source counts above the background

$N_s$  : number of counts in the source region

$b$  :  $\beta N_b$ , area corrected background counts

$\beta$  : ratio of source area to background area

$N_b$  : number of counts in the background region

The flux limit at which a detection would be possible can be found by first calculating the number of source counts required for a  $3\sigma$  detection in each of the observations. The source counts above the background were calculated using Equation 6.1 and were found to be 57 and 55 for XMM-1 and XMM-2 respectively. Though the XMM-1 observation is 3.4ks long and the unfiltered XMM-2 observation was 19ks, the same approximate number of source counts are required for a detection due to a higher level of background in XMM-1. The flux limit was estimated using the HEASARC tool `WebPIMMS`<sup>5</sup>. The HEASARC tool requires a count rate and spectral parameters in order to approximate the flux. The spectral parameters used in the flux estimate are those for the absorbed power-law in Table 6–2. The flux

---

<sup>5</sup> see: <http://heasarc.gsfc.nasa.gov/Tools/w3pimms.html>

upper limits for XMM-1 and XMM-2 were found to be  $\leq 8.29 \times 10^{-14}$  erg cm $^{-2}$  s $^{-1}$  and  $\leq 1.45 \times 10^{-14}$  erg cm $^{-2}$  s $^{-1}$  respectively; a factor of 10 fainter than the detection with *Chandra*.

### 6.3.3 Aql X-1

Activity from Aql X-1 that could be associated with a  $\sim$  msec radio burst was investigated in the 11 *Chandra* observations. From each of the L1 event files, source counts associated with PI channels were extracted from a circular region of 5 arcsec radius centered on Aql X-1. The background was also extracted from each of the 11 *Chandra* observations from a circle of 33 arcsec far from the source, this was the maximum size of a circle which could be made. All the counts in each PI channel were summed from each observation for the source and the background. Then the PI channels were binned such that 16 channels became one bin. Figure 6-3 displays the total number of area corrected counts in the binned PI channels from the source and background regions. In the highest binned PI channel there are a total of 48 counts from the Aql X-1 regions (source plus background) and 38 background region area corrected counts. Treating the background counts as the mean, the probability of getting 48 counts or more is 7% using the Poisson probability distribution. Thus, no significant counts in the high PI channel are found in excess of that expected from the background.

## 6.4 Discussion

An unidentified source was detected in the *Chandra* observation 709. This source has no catalogued spatially coincident counterpart in either the 2MASS All-sky survey, or USNO-B1.0 catalogues. The detected source is designated CXOU

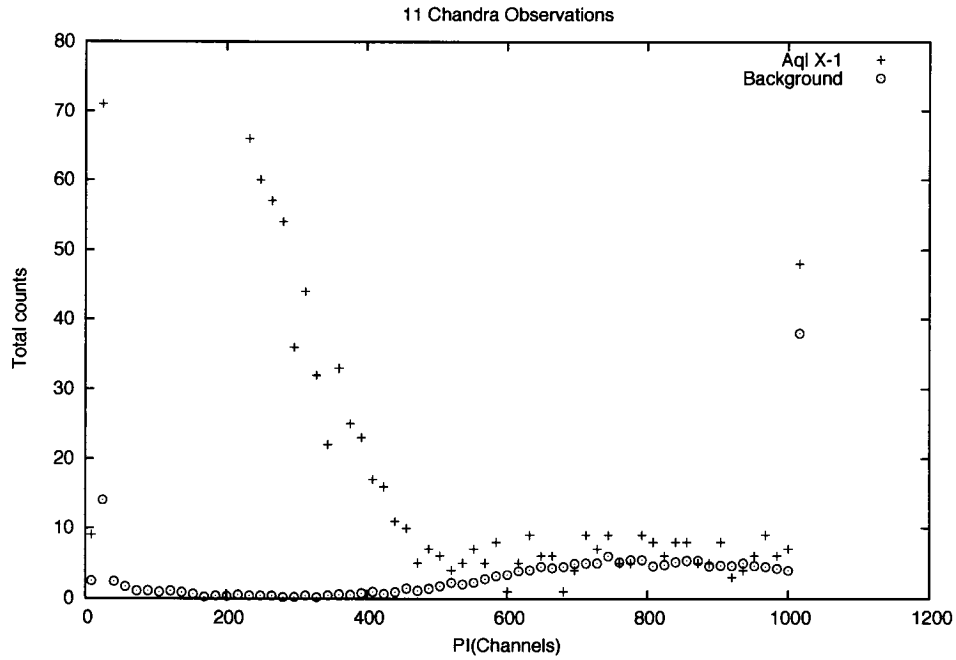


Figure 6–3: The added counts in the PI channels for all the *Chandra* Aql X-1 observations along with adding the background from each of the observations. The PI channels were linearly binned by a factor of 16 to have 64 bins in the end. The background counts have been area corrected to the area of the Aql X-1 extraction region.

J191121.4+003844. CXOU J191121.4+003844, was not in the field of view in any of the other *Chandra* observations.

The spectrum of CXOU J191121.4+003844 is best described by an absorbed power-law ( $\alpha=1.0_{-0.4}^{+0.3}$ ). CXOU J191121.4+003844, was not detected in either of the *XMM-Newton* observations, which indicates a transient nature.

Both CXOU J191121.4+003844 and Aql X-1 fell within the error circle of RRAT J1911+00 (McLaughlin et al., 2005, see). No new activity was detected from Aql X-1. CXOU J191121.4+003844 with its proximity to the RRAT J1911+00, not being listed in either the 2MASS or USNO-B1-0 catalogues, being characterized by a non-thermal spectrum and the possible transient nature makes CXOU J191121.4+003844, a candidate counterpart to RRAT J1911+00, worthy of further study.

## CHAPTER 7 Conclusions

### 7.1 *XMM-Newton* Observations

During the *XMM-Newton* observations, Aql X-1 was not in quiescence. A luminosity on the order of  $10^{36}$  erg cm<sup>-2</sup> s<sup>-1</sup> was measured during both observations, three orders of magnitude higher than the quiescent luminosity, below the typical outbursting luminosity, suggesting Aql X-1 was accreting at an intermediate rate, between quiescent and an outbursting rate. Also, the XMM-1 observation had a flux  $\sim 2$  times brighter than the XMM-2 observation. The XMM-1 observation was best described by an absorbed blackbody and the XMM-2 with the lower flux was best described by an absorbed blackbody with a power-law component. Thus, Aql X-1 was not in a suitable state for radius measurements using hydrogen atmosphere modeling.

### 7.2 Search for Spectral lines

The presence of spectral lines in the two *XMM-Newton* observations was investigated using observations taken with the RGS instrument. There was no visual evidence for emission lines.

### 7.3 Radius Measurements

Using the individual spectra of Aql X-1 from the 11 *Chandra* observations, radius measurements were made. A spectral model of an absorbed hydrogen atmosphere was used for the spectral fitting. Of the 11 *Chandra* observations, 8 spectra were

described to a statistically acceptable level with the model. However, 3 were not consistent with a hydrogen atmosphere model alone, likely indicating the presence of a high-energy ( $>2\text{keV}$ ) spectral component.

All 11 *Chandra* spectra were fit simultaneously. It was found that constant absorption and thermal components with a varying high energy component best describe the observations. A power-law was used to parameterize the high energy component. With increasing count rate (intensity) the power-law index decreased and the power-law normalization increased.

From the jointly fit 11 *Chandra* observations the best fit neutron star radius measurement for Aql X-1 was  $R_\infty = 11.6_{-0.1}^{+0.4} \text{km}$  ( $d/5\text{kpc}$ ). The best fit  $\text{Log}T_{eff}(\text{K}) = 6.49_{-0.02}^{+0.01}$  and  $R_\infty$  are from applying a constant thermal component and a varying power-law component. The errors on the best fit  $R_\infty$  do not include the uncertainty in the distance to Aql X-1, which is now the dominant uncertainty in the radius measurement. Using this radius measurement and assuming a mass, dEOSs can be excluded as being acceptable descriptions of dense matter at the center of a neutron star. As an example, with the assumption that the distance to Aql X-1 as 5kpc and the mass is  $1.4M_\odot$  the EOS labeled MS0, MS1, GM3, and AP4 in figure 1-1 can be excluded. This radius measurement makes improvement in the Aql X-1 distance measurement an important next step in further pinning down the neutron star radius measurement and thusly the dEOS.

#### 7.4 RRATs

In the Chandra observation 709, an unidentified source was detected. This source was not found listed in the 2MASS All-sky catalogue, or the USNO-B1.0 catalogue. The source was designated CXOU J191121.4+003844. CXOU J191121.4+003844 was not detected in the two XMM-Newton observations, which is an indication of a transient nature. CXOU J191121.4+003844 as well as Aql X-1 both fell within the error circle of the RRAT J1911+00. No new activity was detected from Aql X-1. CXOU J191121.4+003844 is worthy of further study due to: its proximity to RRAT J1911+00, characterization by a non-thermal spectrum and transient nature.

## Appendix: Abbreviations

ACIS: Advanced CCD Imaging Spectrometer

Aql X-1: Aquila X-1

ASCA: Advanced Satellite for Cosmology and Astrophysics

ASM: All Sky Monitor

BI: Back Illuminated

CALDB: Chandra Calibration Database

CIAO: Chandra Interactive Analysis of Observations

CIF: Calibration Index File

dEOS: dense mater Equation of State

EPIC: European Photon Imaging Camera

FI: Front Illuminated

FOV: Field of View

FPCS: Focal Plane Crystal Spectrometer

GIS: Gas Imaging Spectrometer

GTI: Good Time Interval

HETG: High Energy Transmission Grating

HRC: High Resolution Camera

HRI: High Resolution Imager

IPC: Imaging Proportional Counter

LETG: Low Energy Transmission Grating

MOS: Metal Oxide Semi-conductor

ODF: Observation Data File  
OM: Optical Monitor  
PPS: Pipeline Processing Subsystem  
qLMXB: quiescent Low-Mass X-ray Binary  
RFC: RGS Focal Camera  
RGA: Reflection Grating Assembly  
RGS: Reflection Grating Spectrometer  
ROSAT: ROentgen SATellite  
RRAT: Rotating RAdio Transient  
RXTE: Rossi X-ray Timing Explorer  
SAS: Science Analysis Software  
SIS: Solid-state Imaging Spectrometer  
SXT: Soft X-ray Transient  
TOA: Time Of Arrival  
XMM: X-ray Multi-Mirror mission

## References

- Asai, K., Dotani, T., Hoshi, R., Tanaka, Y., Robinson, C. R., & Terada, K., 1998, *Publ.Astron.Soc.Japan* 50, 611
- Bevington, P. & Robinson, D., 2003, "*Data Reduction and Error Analysis for the Physical Sciences*", McGraw-Hill
- Brown, E. F., Bildsten, L., & Rutledge, R. E., 1998, *Ap.J.* 504, L95
- Cackett, E. M., Wijnands, R., Heinke, C. O., Edmonds, P. D., Lewin, W. H. G., Pooley, D., Grindlay, J. E., Jonker, P. G., & Miller, J. M., 2005, *Ap.J.* 620, 922
- Campana, S., Israel, G. L., Stella, L., Gastaldello, F., & Mereghetti, S., 2004, *Ap.J.* 601, 474
- Campana, S., Mereghetti, S., Stella, L., & Colpi, M., 1997, *Astronomy & Astrophysics* 324, 941
- Campana, S. & Stella, L., 2003, *Ap.J.* 597, 474
- Campana, S., Stella, L., Mereghetti, S., Colpi, M., Tavani, M., Ricci, D., Fiume, D. D., & Belloni, T., 1998, *Ap.J. (Letters)* 499, L65+
- Chevalier, C., Ilovaisky, S. A., Leisy, P., & Patat, F., 1999, *Astronomy & Astrophysics* 347, L51
- Colpi, M., Geppert, U., & Page, D., 2000, *Ap.J. (Letters)* 529, L29
- Cottam, J., Paerels, F., & Mendez, M., 2002, *Nature* 420, 51
- Cui, W., Barret, D., Zhang, S., Chen, W., Boirin, L., & Swank, J., 1998, *Ap.J.* 502,

- Czerny, M., Czerny, B., & Grindlay, J. E., 1987, *Ap.J.* 312, 122
- den Herder, J. W., Brinkman, A. C., Kahn, S. M., Branduardi-Raymont, G., Thomsen, K., Aarts, H., Audard, M., Bixler, J. V., den Boggende, A. J., Cottam, J., Decker, T., Dubbeldam, L., Erd, C., Goulooze, H., Güdel, M., Guttridge, P., Hailley, C. J., Janabi, K. A., Kaastra, J. S., de Korte, P. A. J., van Leeuwen, B. J., Mauche, C., McCalden, A. J., Mewe, R., Naber, A., Paerels, F. B., Peterson, J. R., Rasmussen, A. P., Rees, K., Sakelliou, I., Sako, M., Spodek, J., Stern, M., Tamura, T., Tandy, J., de Vries, C. P., Welch, S., & Zehnder, A., 2001, *Astronomy & Astrophysics* 365, L7
- Ebisawa, K., Bourban, G., Bodaghee, A., Mowlavi, N., & Courvoisier, T. J.-L., 2003, *Astronomy & Astrophysics* 411, L59
- Gendre, B., Barret, D., & Webb, N., 2003a, *Astronomy & Astrophysics* 403, L11
- Gendre, B., Barret, D., & Webb, N. A., 2003b, *Astronomy & Astrophysics* 400, 521
- Giacconi, R., Kellogg, E., Gorenstein, P., Gursky, H., & Tananbaum, H., 1971, *Ap.J. (Letters)* 165, L27+
- Harmon, B. A., Wilson, C. A., Tavani, M., Zhang, S. N., Rubin, B. C., Paciesas, W. S., Ford, E. C., & Kaaret, P., 1996, *Astron. Astrophys. Suppl. Ser.* 120, C197+
- Hasinger, G., Altieri, B., Arnaud, M., Barcons, X., Bergeron, J., Brunner, H., Dadina, M., Dennerl, K., Ferrando, P., Finoguenov, A., Griffiths, R. E., Hashimoto, Y., Jansen, F. A., Lumb, D. H., Mason, K. O., Mateos, S., McMahon, R. G., Miyaji, T., Paerels, F., Page, M. J., Ptak, A. F., Sasseen, T. P., Schartel, N., Szokoly, G. P., Trümper, J., Turner, M., Warwick, R. S., & Watson, M. G., 2001,

- Astronomy & Astrophysics* 365, L45
- Heger, A., Fryer, C. L., Woosley, S. E., Langer, N., & Hartmann, D. H., 2003, *Ap.J.* 591, 288
- Ilovaisky, S. & Chevalier, C., 2004, *Astron. Telegram* 260
- Juett, A. M. & Chakrabarty, D., 2003, *Ap.J.* 599, 498
- Kaluzienski, L. J., Holt, S. S., Boldt, E. A., & Serlemitsos, P. J., 1977, *Nature* 265, 606
- Koyama, K., Inoue, H., Makishima, K., Matsuoka, M., Murakami, T., Oda, M., Osgawara, Y., Ohashi, T., Shibasaki, N., Tanaka, Y., Marshall, F. J., Kondo, I. S., Hayakawa, S., Kunieda, H., Makino, F., Masai, K., Nagase, F., Tawara, Y., Miyamoto, S., Tsunemi, H., & Yamashita, K., 1981, *Ap.J. (Letters)* 247, L27
- Lasota, J.-P., 2001, *New Astronomy Review* 45, 449
- Lattimer, J. M. & Prakash, M., 2001, *Ap.J.* 550, 426
- Lattimer, J. M. & Prakash, M., 2004, *Science* 304, 536
- Levine, A. M., Bradt, H., Cui, W., Jernigan, J. G., Morgan, E. H., Remillard, R., Shirey, R. E., & Smith, D. A., 1996, *Ap.J. (Letters)* 469, L33
- Lewin, W. H., van Paradijs, J., & Taam, R., 1995, in J. Lewin, Walter H.G. and van Paradijs & E. P. van den Heuvel (eds.), *X-Ray Binaries*, pp 175–232
- Li, B.-A. & Steiner, A. W., 2005, *nucl-th/0511064*
- Maccarone, T. J. & Coppi, P. S., 2003, *Astronomy & Astrophysics* 399, 1151
- Maitra, D. & Bailyn, C. D., 2004, *Ap.J.* 608, 444
- Manchester, R. N., 2004, *Science* 304, 542
- McLaughlin, M. A., Lyne, A. G., Lorimer, D. R., Kramer, M., Faulkner, A. J.,

- Manchester, R. N., Cordes, J. M., Camilo, F., Possenti, A., Stairs, I. H., Hobbs, G., D'Amico, N., Burgay, M., & O'Brien, J. T., 2005, *astro-ph/0511587*
- Monet, D. G., Levine, S. E., Canzian, B., Ables, H. D., Bird, A. R., Dahn, C. C., Guetter, H. H., Harris, H. C., Henden, A. A., Leggett, S. K., Levison, H. F., Luginbuhl, C. B., Martini, J., Monet, A. K. B., Munn, J. A., Pier, J. R., Rhodes, A. R., Riepe, B., Sell, S., Stone, R. C., Vrba, F. J., Walker, R. L., Westerhout, G., Brucato, R. J., Reid, I. N., Schoening, W., Hartley, M., Read, M. A., & Tritton, S. B., 2003, *A.J.* 125, 984
- Paerels, F., 1997, *Ap.J. (Letters)* 476, L47+
- Pavlov, G. G., Shibanov, I. A., & Zavlin, V. E., 1991, *M.N.R.A.S.* 253, 193
- Pivovarov, M. J., 2000, *Ph.D. thesis*, Massachusetts Institute of Technology
- Priedhorsky, W. C. & Terrell, J., 1984, *Ap.J.* 280, 661
- Reynolds, S. P., Borkowski, K. J., Gaensler, B. M., Rea, N., McLaughlin, M., Possenti, A., Israel, G., Burgay, M., Camilo, F., Chatterjee, S., Kramer, M., Lyne, A., & Stairs, I., 2005, *astro-ph/0512379*
- Rodriguez, J., Hannikainen, D., & Mowlavi, N., 2004, *Astron. Telegram* 280
- Rodriguez, J., Shaw, S. E., & Corbel, S., 2006, *Astronomy & Astrophysics* 451, 1045
- Rutledge, R. E., Bildsten, L., Brown, E. F., Pavlov, G. G., & Zavlin, V. E., 2001a, *Ap.J.* 559, 1054
- Rutledge, R. E., Bildsten, L., Brown, E. F., Pavlov, G. G., & Zavlin, V. E., 2001b, *Ap.J.* 551, 921
- Rutledge, R. E., Bildsten, L., Brown, E. F., Pavlov, G. G., & Zavlin, V. E., 2002a, *Ap.J.* 578, 405

- Rutledge, R. E., Bildsten, L., Brown, E. F., Pavlov, G. G., & Zavlin, V. E., 2002b, *Ap.J.* 577, 346
- Rutledge, R. E. & Sako, M., 2003, *M.N.R.A.S.* 339, 600
- Skrutskie, M. F., Cutri, R. M., Stiening, R., Weinberg, M. D., Schneider, S., Carpenter, J. M., Beichman, C., Capps, R., Chester, T., Elias, J., Huchra, J., Liebert, J., Lonsdale, C., Monet, D. G., Price, S., Seitzer, P., Jarrett, T., Kirkpatrick, J. D., Gizis, J. E., Howard, E., Evans, T., Fowler, J., Fullmer, L., Hurt, R., Light, R., Kopan, E. L., Marsh, K. A., McCallon, H. L., Tam, R., Van Dyk, S., & Wheelock, S., 2006, *A.J.* 131, 1163
- Thorsett, S. E. & Chakrabarty, D., 1999, *Ap.J.* 512, 288
- Tiengo, A., Galloway, D. K., di Salvo, T., Méndez, M., Miller, J. M., Sokoloski, J. L., & van der Klis, M., 2005, *astro-ph/0506590*
- Ushomirsky, G. & Rutledge, R. E., 2001, *M.N.R.A.S.* 325, 1157
- van Paradijs, J. & Lewin, W. H. G., 1987, *Astronomy & Astrophysics* 172, L20
- van Paradijs, J., Verbunt, F., Shafer, R. A., & Arnaud, K. A., 1987, *Astronomy & Astrophysics* 182, 47
- Verbunt, F., Belloni, T., Johnston, H. M., van der Klis, M., & Lewin, W. H. G., 1994, *Astronomy & Astrophysics* 285, 903
- Welsh, W. F., Robinson, E. L., & Young, P., 2000, *A.J.* 120, 943
- White, N., Nagase, F., & Parmar, A., 1995, in W. H. Lewin, J. van Paradijs, & E. P. van den Heuvel (eds.), *X-Ray Binaries*, pp 1–57
- Zavlin, V. E. & Pavlov, G. G., 2002, in W. Becker, H. Lesch, & J. Trümper (eds.), *Neutron Stars, Pulsars, and Supernova Remnants*, pp 263–+

Zavlin, V. E., Pavlov, G. G., & Shibanov, Y. A., 1996, *Astronomy & Astrophysics*  
315, 141